Intensified paraglacial slope failures due to accelerating downwasting of a temperate glacier in Mt. Gongga, Southeast Tibet Plateau

Yan Zhong[1,2], Qiao Liu[1], Matthew Westoby[3], Yong Nie[1], Francesca Pellicciotti[4], Bo Zhang[5], Jialun Cai[5], Guoxiang Liu[5], Haijun Liao[1,2], Xuyang Lu[1]

[1] Institute of Mountain Hazards and Environment, Chinese Academy of Sciences, Chengdu 610041, China
[2] College of Resources and Environment, University of Chinese Academy of Sciences, Beijing 100049, China
[3] Department of Geography and Environmental Sciences, Engineering and Environment, Northumbria University, Newcastle upon Tyne NE1 8ST, UK
[4] Swiss Federal Institute for Forest, Snow and Landscape Research WSL, 8903 Birmensdorf, Switzerland
[5] Department of Surveying and Geo-Informatics, Faculty of Geosciences and Environmental Engineering, Southwest Jiaotong University, Chengdu 611756, China

Correspondence to: Qiao Liu (liuqiao@imde.ac.cn)

Abstract. Topographic development via paraglacial slope failure (PSF) represents a complex interplay between geological structure, climate, and glacial denudation. Where debris generated by PSFs is deposited on the surface of a glacier, this debris can increase the extent or thickness of a supraglacial debris-cover, in turn modifying glacier ablation and affecting meltwater generation. This study pays attention to the intensity and frequency of PSFs in a glacierised, monsoon temperate region of Southeast Tibet Plateau (SETP), a region that has experienced the most remarkable accelerating ice mass loss among High Mountain Asia (HMA) during past decades. In our case, we mapped PSFs along the 5 km-long, 0.5 km-width, west-east trending ice tongue of Hailuogou Glacier (HLG), a well-monitored monsoon temperate valley glacier in Mt. Gongga, using repeat satellite- and unpiloted aerial vehicle (UAV)-derived imagery between 1990 and 2020. Accompanying with the observed glacier retreat and thinning, the overall paraglacial bare ground area (PBGA) increased from 0.31±0.27 km^2 in 1990 to 1.38±0.06 km^2 in 2020, with decadal expansion rates from ~0.01 km^2 a^{-1} in 1990-2000 and 0.02 km^2 a^{-1} in 2000-2011, to 0.08 km^2 a^{-1} in 2011-2020, indicating an intensified paraglacial failure process. Three types of PSF, including (A) rockfall, (B) sediment-mantled slope slide, and (C) gully headward erosion, with a total area of 0.75±0.03 km^2 in 2020, were identified and documented based on recently repeating high-resolution UAV mappings. The formation, evolution, and current status of these typical PSFs are generally related to the history of glacier dynamics and paraglacial geomorphological adjustments, and also influenced and/or disturbed by the fluctuation of air temperature/precipitation and their combinations. Despite a slightly decreasing trend of annual precipitation was observed at our studied site, the absolute high-amount precipitation in Mt. Gongga as well as other monsoon-dominated deglaciating mountain areas must have played important roles in the intensified denudation, nested processes, and failure of the paraglacial slopes.

1 Introduction

The thinning and retreat of mountain glaciers exposes new, unstable landscapes which are susceptible to rapid geomorphological changes (i.e., with a high entropy). Sparsely vegetated or unvegetated drift-mantled slopes are particularly susceptible to be modified by gravitational, aeolian, and fluvial processes and rapidly reworked by debris flows, rock avalanches, and slope-wash (Ballantyne, 2003;Ballantyne, 2002;Deline et al., 2015a;Eichel et al., 2013). Glacier downwasting can destabilize slopes through undercutting and, simultaneously, the progressive loss of buttress exerted by ice loading on its adjacent slopes may result in rock stress-releases, scilicet "debuttressing", altering the state of stress that exists within the slope accordingly. Such slope failures initiate four possible modes of response: (1) large-scale catastrophic rock slides and rock avalanches (Kirkbride and Deline, 2018;Fischer et al., 2010); (2) ice-contact slope movements (McColl and Davies, 2013); and (3) periodic small-scale rock topples or rockfalls (Cook et al., 2013); and (4) deep-seated gravitational creep (Deline et al., 2015b;Ballantyne et al., 2014). These four types of response provide a useful framework for examining the processes and geomorphological consequences of slope adjustment after deglaciation. These responses can be further divided into two types: rock slope failures and sediment slope failures, which are usually described collectively as paraglacial slope failures (PSFs). PSFs encompass failure of steep rock walls and lateral moraine slopes following glacier downwasting (Church and Ryder, 1972;Fickert and Grüninger, 2018) and are widely distributed in deglaciating or deglaciated landscapes. PSFs constitute a key mechanism for rapid degradation of recently glacial landscapes, as they contribute to the disaggregation of large portions of valley sides and the transformation from U-shaped to V-shaped valleys. High-frequency, low-magnitude PSFs can transport a considerable volume of debris onto glacier surfaces (Smith et al., 2020), thereby facilitating the accumulation of the supraglacial moraine. Because thin debris covers enhance ablation, whilst thicker covers suppress it (Fyffe et al., 2020), debris supply dynamics ultimately affect glacial ablation and meltwater production (Rowan et al., 2018). In addition, accompanied by relatively rare but occasional rainstorm events, those unsorted debris are very likely transformed into debris flows and cascading geo-disasters that threaten downstream infrastructure, freshwater availability, and the safety of residents and tourists (Hewitt et al., 2011;Reznichenko et al., 2012).

Monsoonal temperate glaciers in the Southeast Tibetan Plateau (SETP) have experienced higher rates of mass loss and ice thinning than other High Mountain Asia (HMA) glacierized regions in past decades (Neckel et al., 2017;Brun et al., 2017). In addition to seismically active, the combination of high-intensive glacier ablation and abundant/extremely monsoonal precipitation make SETP one of the most susceptible regions of the glacier or water-related geo-hazards (Yao et al., 2019a), such as glacial debris flow, ice/snow avalanche, glacier-related landslide, and glacial lake outburst flood (Fan et al., 2019;Cheng et al., 2010;Xu et al., 2012). For example, at least four glacier-related landslides (1990-2018, (Liu et al., 2010;He et al., 2008;Pan et al., 2012;Cao et al., 2019;Liu et al., 2018;Liu and Liu, 2010)), and 12 glacial lake outburst floods (1931-2014, (Liu et al., 2019b;Yao et al., 2014)) have been recorded across the SETP. Mass movements resulting from large-scale slope failures routinely form temporary valley-blocking natural dams (Liu et al., 2019c), behind which large lakes can develop

and eventually outburst. Mass movements originated from tributary valleys where glacier recession and permafrost thaw have reduced slope stability has likely contributed to these large-scale slope failures (Zou et al., 2020;Korup et al., 2010). It was also suggested that more than half of the debris flows recorded in the SETP were cryogenic (Hu et al., 2011). Glacier destabilization itself was also one of the concerned sources of the cascade hazard events, such as historically reported surge induced catastrophes (Zhang, 1985) and recent ice avalanche induced debris flow that blocks the Yarlung Tsangpo river (Chen et al., 2020;Kääb et al., 2021). These cascading geo-hazards have caused severe economic losses or some heavy casualties to SETP local communities.

With populations and economies expanding, it is anticipated that the magnitude and frequency of glacier-related hazard in the SETP will increase in near future (Yao et al., 2019b) since the accelerating glacial mass loss and permafrost degradation due to climate warming will continue to destabilize the paraglacial landscapes (McColl, 2012). While a growing body of studies focusing on the process of paraglacial hillslopes destabilization in the European Alpine (Curry et al., 2006;Kirkbride and Deline, 2018), Southern Alps (Cody et al., 2020;McColl, 2012), Cordillera Blanca (Andes) (Emmer et al., 2020) and Himalayas (van Woerkom et al., 2019), yet few cases have been reported for the transient condition of paraglacial slopes in the deglaciating SETP. In this study, we select the Hailuogou Glacier (HLG, a monsoon temperate glacier in Mt. Gongga that has been well documented and observed since the early 20th century) as a detailed case site to study the interactions between glacier shrinkage and paraglacial slope adjustments during the past decades. Our investigations are based on the analysis of historical satellite images and recent field-based high-resolution phototopography mappings using unpiloted aerial vehicle (UAV), combined with in-situ geomorphological observations and measurements. The main objectives of this research are to: (A) map and quantify the spatiotemporal variability of PSFs around the lower tongue of HLG based on time-series image comparison; (B) classify the PSFs, analyse their topographic conditions, and discuss their possible physical mechanisms; (C) discuss the geomorphic and environmental effects of these slope processes by exploring the possible linkage between climate change, glacier downwasting and PSFs in a typical monsoon-dominated region characterised by accelerated glacial and paraglacial denudation.

2 Study area

Hailuogou Glacier (29°58.4′N, 101°91.6′E) is one of the largest debris-covered valley glaciers in the Mt. Gongga region (Fig. 1). It is a ~13 km-long, east-facing monsoon temperate glacier, has an area of 24.7 km², and extends in altitude from 2990 m to 7556 m a.s.l. The glacier is ~300-500 m in width, and the wider valley is deeply incised below the accumulation area (where the glacier broadens to ~6 km in width). The upper section of the ice tongue (below the icefall) has a surface gradient of ~10° and is connected to very steep (~55°) lateral slopes on both sides. At a distance of ~1.5 km from the base of the icefall (middle section of the ice tongue), the glacier surface steepens to ~12° and becomes highly crevassed. At a distance of 2 km, the glacier turns its flow direction toward the northeast and maintains a surface gradient of ~13° for the remaining 3 km (lower section of

the ice tongue) stretching to the end of the glacier tongue. Paralleling with the lower section of the ice tongue, the height of lateral moraines to the current glacier surface is about 165 m, which is comparatively higher than the further upper glacier (~86 m at the middle section of ice tongue).

The terminus of HLG has retreated more than 2 km since the LIA (Su and Shi, 2002) and this retreat has accelerated from 12.7 m a^{-1} between 1966–1989 to 27.4 m a^{-1} between 1998–2008. Between 1966 and 2009, the mean ice surface elevation of its lower tongue had lowered at a rate of 1.1±0.4 m a^{-1} (Zhang et al., 2010). Due to suitable local thermal (warm) and moisture (wet) climatic conditions, vegetation is able to quickly establish itself on the exposed proglacial bare ground in glacier forelands and lateral moraine slopes, and even on some supraglacial debris-covered areas that are largely stagnant. The LIA preglacial zone (2980-2800 m) is characterized by extremely fast primary vegetation succession and hosts an integrated community ranging from cold-adapted herbaceous species to *Abies fabri* (conifer pine) forest. *Abies fabri* forest patches are also seen along both lateral sides of the ice tongue on the accumulated lateral moraine, which has been relatively stable since the LIA.

Due to its low altitude, easy accessibility, and adjacency to the forests and hot springs, HLG and its surrounding areas have been exploited for tourism since 1987. A glacier ropeway connects the two lateral moraines and transports visitors across the lower part of the ice tongue and provides access to a viewpoint on the southern side of the valley (S2 on Fig. 1) from where the ice tongue can be overlooked and accessed via trail. Between 2000 and 2011, the number of annual visitors increased from 44,000 to 384,000 (Zhu, 2015), and in 2019 the number reached ~2,852,600 (Haiguanju, 2020). The increasing popularity of the glacier comes at a time when tourism facilities and infrastructure are becoming frequently disturbed due to paraglacial landslides, debris flows, and flash floods (Xu et al., 2007;Cai et al., 2021). Beyond the objectives outlined above, there is a need to more fully understand the nature of slope failures in the vicinity so that these failures might be better anticipated, and their potential impacts mitigated where possible.

3 Data and methods

3.1 PSFs mapping and classification

Given a warm and humid climate condition, vegetation colonisation is very fast (1-2 years) in the HLG paraglacial environment. Like many monsoonal temperate glaciers in SETP, the lower part of the HLG tongue and its adjacent slopes are located below the local tree line, any newly developed PSFs could be readily recognized from the changed paraglacial bare ground area (PBGA). We firstly extracted the non-vegetated areas by classifying the land surface with vegetated and unvegetated areas with the Normalized Difference Vegetation Index (NDVI), which was calculated using reflected red and near-infrared band values of satellite images. The PBGAs were then extracted by excluding the glacier-covered areas (GCAs) to generate an initial mapping of PSF. For better inter-annual comparisons, we then manually removed those patches and areas where the PBGA has changed due to vegetation colonisation in some paraglacial slopes and in all glacier foreland to keep the remaining unstable

slope areas as final mapped PSFs. A total of 8 satellite images between 1990 and 2020 (Table 1), including Sentinel-2 (10m), RapidEye (5m), PlanetScope (PL, 3m), were used to extract the PSFs. These data constitute a multi-temporal and dynamic observation of HLG and its surrounding paraglacial environments. Due to the strong influence of the monsoon, the HLG is often covered with thick clouds in summer, rendering 75% of the available summer satellite images unusable. However, we successfully screened and synthesized several Landsat or Sentinel-2 cloudless images in 1990, 2000, 2016, and 2018 using the Google Earth Engine platform. Shadows caused by the relative angle between the sun, ground objects, and sensors will reduce the value of NDVI, but by adjusting the threshold, the vegetated and non-vegetated areas can still be differentiated. Therefore, we used cloudless images in multiple seasons (spring, autumn, and summer) to automatically extract PSFs boundaries. Of the seasonal data, the PSF boundaries extracted from images acquired in the northern hemisphere summer generally suffered less from the terrain shadow than other seasons and can be used directly after validation, and the boundaries extracted from other seasons need to be manually corrected.

To enable more detailed mapping of recent PSF extents, UAV sorties were flown on 31 August 2016, 07 June 2017, and 15 May 2019 using a DJI Phanton 4 Pro UAV, and 19 August 2018 using a DJI Phanton 4 RTK UAV which combination of a global navigation satellite system (GNSS) with a mean horizontal accuracy of 0.01 m + 1 ppm [*] (RMS) in XY (*https://www.dji.com/uk/phantom-4-rtk/info#specs/*), and input photographs were stitched using Structure from Motion (SfM) software ContextCapture Center Master to create a time series of orthomosaic aerial images at 0.1m resolution. However, our earlier UAV surveys were routed with a limited area of off-glacier terrain that was less effectively mapped by photograph overlapping (i.e., section 3.2). This design aspect of the UAV surveys, combined with steeply topographic constraints on the UAV flight area, meant that not all ice-marginal slopes were successfully mapped on the final orthomosaics as well as for the later UAV surveys (Fig. S1). All UAV images are co-registered using an orthorectified PL image acquired on 16 August 2018, which was found to be perfectly co-registered with a 12.5m hills-shade of ALOS PALSAR DEM when manual comparing their topography textures (e.g., terrain ridges and vertexes) from the peak of Mt. Gongga (7556 m a.s.l.) to the trimlines of the glacier close to its terminus (~3000 m a.s.l.). To execute the UAV images co-registration, a total number of 54 features (Fig. S1) were selected as ground control points on stable ground surfaces (e.g., exposed bedrock, trees, or building vertices) on both PL image and UAV images. Their corresponding altitudes were then extracted from the ALOS PALSAR DEM. Overall, the final reported quality of the co-registered UAV images were quite satisfactory (with a total and maximum RMS error of 1.22 and 1.98 pixel respectively, i.e. a mean horizontal error of 0.15 m). An additional error of ±0.5 pixels was estimated to include all the uncertainties of visual interpretation and automatically extracted areas (i.e. multiply linear error and perimeter, e.g. the linear error of Landsat images are 15m, Sentinel 2 images 5 m and PlanetScope images ~1.56 m) (Salerno et al., 2012;Haritashya et al., 2018). Our workflow is summarized in Fig. 2.

[*] 1 ppm means the error has a 1mm increase for every 1 km of movement from the drone.

According to the principles of systematization, standardization, operability, and scalability, the PSF are classified combining the knowledge of the basic slope material composition, erosion type, visual shape, and event magnitude obtained from field investigation and UAV data in HLG, and the classifications proposed by Ballantyne (2002), McColl (2012), Jarman (2006), and Hungr et al. (2014). A classification standard for PSF systems in SETP is proposed, which is divided into two major categories: rock slope failure and sediment slope failure; and five sub-categories: rock avalanches, rockfall, deep-seated gravitational slope deformations, sediment-mantled slope slide, and gulley headward erosion (Tab. S1).

3.2 Slope movement and headscarp erosion rates

To quantify the rate of slope movement between 2016 and 2020, we selected 20-40 points as trackable features of rocks, paths, or infrastructures on a series of UAV mapped slopes (B1-B4 in Fig. S2, Fig. S3). We manually tracked the location of each point in the QGIS software and calculated their mean horizontal displacements annually. For cases that the movement of the slope itself is less notability or extremely low but the headward backwasting is significant, we quantify their rates of headscarp erosion. Based on PSF boundaries delineated on five higher resolution satellite images from 2002 to 2019 (Google Earth SPOT-5 imagery for 2002, RapidEye images 2011, 2014, and 2015, and PlanetScope image 2019), we calculated the mean distance and annual retreat rates for these headscarps using the QGIS Average Nearest Neighbour Analysis procedure.

3.3 Glacier dynamics

Since the evolution of paraglacial slope and their topographic conditions are closely related to the glacier dynamics (Ballantyne and Benn, 1994;Ballantyne, 2002), we thus analysed the geomorphological processes and implications of retreat, thinning, and slowdown of the HLG and their relationships with the PSFs development. Detailed mapping on the retreat and thinning of the HLG over the past decades has been well documented and reported (Li et al., 2010;He et al., 2008;Liu et al., 2018;Zhang et al., 2010;Liu et al., 2010). We extend the boundary of glacier terminus retreat to 2020 using some newly archived satellite images (Fig. 1 and Table 1). We employed the TopoDEM (1966) reported by Zhang et al. (2010), the Shuttle Radar Topography Mission (SRTM, 2000) 30m DEM (Farr et al., 2007), and a calculated 2016 DEM based on the 2000-2016 surface elevation change rate from Brun et al. (2017) to analyse the surface elevation changes of HLG between 1966 and 2016. Surface elevation changes along five profile-lines in longitudinal (A-A' along the glacier central flow line) and transverse (B-B', C-C', D-D', and E-E' perpendicular to the glacier central flow line) on the lower part of HLG (Fig. 1) were examined and compared. The four transverse lines were examined approximately cover every type of PSFs (definition in section 4.2) and a certain distance is maintained in each transverse profile for comparison.

For ice flow dynamics, the earliest observations of surface velocity of the HLG were during 1982-1991 field expeditions, during which the location changes of several stakes along the ice tongue were repeatedly measured. Unfortunately, the original coordinate data of those measurements (e.g., the precise geographic locations of the stakes) was not offered and results are published only as a velocity isoline map with point velocity value indicated. Using 38 SAR images acquired by PALSAR-1/2

satellites from 2007 to 2018, Liu et al. (2019a) extracted annual surface displacement velocities of the HLG between 2007 and 2018. Here we compared the long-term ice flow velocity changes of the HLG (also checked along the five profile-lines mentioned above), based on three-periods results of 1982-1983, 2007-2011, and 2014-2018. The velocity in 1982-1983 is based on a published velocity map (scanned and shown in Fig. S4), which was calculated and extrapolated from in-situ measurements of stake locations using the total station. The velocities during 2007-2011 and 2014-2018 were derived from ALOS/PALSAR satellites using the feature tracking method offered by Liu et al. (2019a).

3.4 Meteorological data

Meteorological conditions nearby the HLG were diagnosed to discuss their possible forcing mechanisms and/or impacts on the development of PSFs. Daily air temperature and precipitation (1988/01/01--2018/12/31) were observed by the Gongga Alpine Ecosystem Observation and Experiment Station (Gongga Mountain Station, 3000 m a.s.l., 2 km to the glacier terminus) with a standard automatic weather station (AWS) installed and managed by the Chinese Ecological Research Network (CERN; *http://www.cern.ac.cn/*). We also collected the manually observed daily temperature data (observed at 2:00 am, 8:00 am, 2:00 pm, 8:00 pm every day by a staff of Mt. Gongga Station) to compensate for the missed AWS data between July and September 2017 due to equipment inspection and between 29 September and 15 October 2018 due to electrical power failures. During the period 1988-2018, the observed mean annual temperature at 3000 m a.s.l. was 4.5 ℃. Rain gauge recorded an average annual number of 314 days and a mean annual amount of 1912 mm precipitation, of which 88% amount was concentrated in ablation seasons (April to October) and ~42% was concentrated in summer (July to September).

4 Results

4.1 Retreating, thinning, and deceleration of the HLG

Glacier outlines in 2002, 2016, and 2020 (Fig. 1c) were manually delineated based on high resolution images (Google Earth SPOT-5 imagery for 2002, UAV images for 2016, and PL imagery for 2020). Comparison of these outlines shows that the glacier tongue area has reduced from 2.30±0.06 km^2 to 1.95±0.02 km^2 (average 0.09±0.03 km^2 a^{-1}) between 2016 and 2020 compared with the period 2002-2016 when it reduced from 2.65±0.01 km^2 to 2.30±0.06 km^2 (average 0.03±0.01 km^2 a^{-1}). Between 2002 and 2016, the position of the glacier terminus showed a moderate retreat (6±0.44 m a^{-1}); whereas during the following four years (2016-2020), the terminus retreated more than 220±1.56 m (~54±0.39 m a^{-1}). Field observations indicate that the current glacier terminus area was no longer covered by thicker debris as previous status, and frequent collapse along the subglacial outlet channel became the major backwasting process causing the accelerated terminus retreat.

The lower part of the HLG tongue also showed continuous narrowing as it retreats due to ice thinning. Ice surface elevation and velocity along five profile lines (Fig. 3) show that the ice tongue has experienced substantial ice loss and slowdown over the past decades. The longitudinal line (A-A') along the glacial flow direction runs through the entire ablation zone. Between

1966 and 2000, we observed negligible to small changes in the surface elevation of the upper ice tongue (-0.5~0 m a^{-1}, between 3400 to 3700 m a.s.l), with a mean lowering the rate of -0.11 m a^{-1}. However, the ice tongue below 3200 m a.s.l (3~4.5 km to the base of the icefall) thinned remarkably as the highest lowering rate up to -2.2 m a^{-1} near the glacier terminus. In contrast, the thinning rate of the upper ice tongue has greatly increased between 2000 and 2016, with the surface elevation change rate remaining at around -2.0 m a^{-1}. On the other hand, the lower part of the ice tongue (below 3400m) shows a decreasing thinning rate towards the terminus. For transverse profiles B-B' and C-C', rates of surface elevation lowering were much higher during 2000-2016 (-1.8 m a^{-1}) than 1966-2000 (-0.3~0 m a^{-1}). In contrast, profiles D-D' and E-E' showed less surface lowering over the past 50 years, with thinning rates remaining around -0.6 m a^{-1} and -0.9 m a^{-1}, respectively.

Analysis of ice surface velocities during three periods (1982-1983, 2007-2011, and 2014-2018) in the past 38 years (Fig. 3c) indicates that the lower ablation area of HLG has experienced a gradual slowdown, with the rate of this deceleration decreasing of glacier (Fig. 3c, profile A-A') and with increasing proximity to the lateral margins (Fig. 3c, profiles B-E). Ice surface velocities along all transverse cross sections have gradually decreased, with the greatest deceleration occurring along with profiles B-B' to D-D' (mean rate of 0.26 m a^{-1}) and less along the E-E' section (mean rate of 0.06 m a^{-1}). Note that remarkable decelerations that happened across the whole transverse profile of D-D' during our observation periods have led the ice tongue below almost stagnated (with a velocity less than 0.1 m a^{-1}) during 2014-2018.

4.2 Paraglacial slope failures

Mapped extents of the PBGAs between 1990 and 2020 were presented in Fig. 4. The PBGA show continual expansion during the observation period, increased from 0.31±0.27 km^2 in 1990 to 1.38±0.06 km^2 in 2020, with a total areal increase of 1.07±0.32 km^2. Its decadal expansion rates increased from ~0.01 km^2 a^{-1} in 1990-2000 and 0.02 km^2 a^{-1} in 2000-2011, to ~0.08 km^2 a^{-1} in 2011-2020, which was approximately proportionate to the annual decrease in the GCA. Due to a transient rockfall below the icefall occurred between September and November 2018, the PBGA increased significantly, with an expansion rate up to ~0.11 km^2 a^{-1} (10.43%) from 2018-2019 within one year. In general, the north-facing slope (located on the true right side of the glacier) exhibits more stability than the south-facing slope, where 56% of the total PBGA was mapped.

According to the classification method in Tab. S1, we identified three typical styles of paraglacial slope failure within the PBGA, with a total area of 0.75±0.03 km^2 in 2020 (Fig. 5a):

A. Rockfall, 0.06±0.01 km^2 in 2020, 8% of the total PSF area.
B. Sediment-mantled slope slide, 0.37±0.01 km^2 in 2020, 49% of the total PSF area.
C. Gully headward erosion, 0.32±0.01 km^2 in 2020, 43% of the total PSF area.

Based on the calculated surface slope map from the 2016 DEM (Fig. S5) as well as field verifications (Fig. S6), the Type B and C PSFs (with a mean surface slope of 29° and 32°, respectively) usually show lower slopes in their unstable areas than stable areas (40-60°). The mean slope of the Type A PSF is about 54°, which is within the range of the stable slope. Below we will present a detailed descriptive analysis for each type of PSF observed at HLG and provide a summary of the dimension and typology for each specific PSF identified in Fig. 5a in Table 2.

4.2.1 Rockfall (PSF type A)

Different magnitude rockfalls are common at exposed steep bedrock terrain on both sides of HLG. A recent large rockfall event (Type A, Fig. 5b) was occurred around October 15 2018 originating from a south-facing paraglacial slope high-hanging above the upper HLG ice tongue (4000 m a.s.l., ~450 m high from the glacier surface). The rockfall deposit and the existing glacier debris cover are slightly different in colour and grain size and can thus be clearly delineated on the glacier surface, both on field photograph and on remote sensing imagery (Fig. 5b and Fig. S7). The deposition area of the rockfall covers a projected area of ~47,000 m^2, stretching a vertical height of 380 m and slope length of 472 m (runout length ~365 m). Based on the extent of the main detachment zone, the deposition thickness (3-5 m estimated during the field visit) and area (Fig. 5b), the total release volume of the rockfall is 1,000-10,000 m^3. We also observed several suspected major rockfall scars on the lower part of the valley wall in close proximity to this scar deposit (i.e., up to 260~400 m above the glacier surface; Fig. 5b and 5c) suggesting that numerous similar scale rockfalls have occurred in this locality. Since the rock surface has been partially weathered and most of the bedrock has been covered by vegetation such as mosses and shrubs, we speculate that these rockfalls may have occurred earlier and have not been documented by remote sensing images or literature.

Except for the 2018 large rockfall, we identified at least 15 fresh small-magnitude rockfalls in view of their evident talus depositions based on UAV images and field investigation (Fig. 5a, Fig. S7). These small-scale rockfalls are found located on both sides of the lower paraglacial slopes and have a source area ranging from 59 to 3028 m^2. Their disintegrating rocks were located between 3100 and 3500 m a.s.l. with a mean vertical distance of about 110 m from their lowest breakpoints to the glacier surface. Unfortunately, due to their small sizes and without continuous observations (e.g., time-lapse photography), we cannot determine the exact time when they happened. These collapsed rocks falling on the glacier surface with different magnitude obviously are one of the important inputs for supraglacial debris on the lower part of the HLG ice tongue.

4.2.2 Sediment-mantled slope slide (PSF type B)

We identified evidence of four major sediment-mantled slope slides (Type B, B1-B4, Fig. 5a). Combined, these features cover an area of ~370,000 m^2 (2019-PL) and are located on both north- and south-facing valley sides. The 2D area of Type B PSFs steadily expanded through four processes: glacier downwasting exposing more of the slope, lateral expansion of the failure mass, and headward expansion from retrogressive failure or degradation of the scarp, over our monitoring period (Fig. 4). The total area increased by 297,000 m^2 and the area expansion rate was 10.16% a^{-1} from 1990 to 2020.

B1 (3500 m a.s.l, Fig. S2a) is located on a north-facing lateral moraine slope at a distance of 1.5 km from the base of the icefall and is 114 m wide, 1035 m long, and 112,424 m^2 in area. Between 2017 and 2019 the exposed area of this feature B1 slope increased by 12,125 m^2, or a percentage increase of 12.09 %. A landslide with an area of 53,000 m^2 is included as a nested feature within B1 (48.28% of B1 area), and evidence of superimposed gullying is also found on the eastern, western, and northern segments of this feature. The UAV images in 2016 did not cover the B1 area completely, so we extracted 23 common tie points across UAV images from 2017 to 2019 to manually quantify the surface displacement rate; the slope showed downslope displacement of 1.96±0.04 cm d^{-1}, and a maximum of 2.08±0.04 cm d^{-1} in the period 2017-2018.

Feature B2 (3150 m a.s.l, Fig. S2b) is the largest type B PSF and is located on the true left, south-facing moraine slope close to the glacier terminus (3240-3120 m a.s.l.). It is fan-shaped with a width of ~262 m, a length of 644 m, a height of ~120 m, and a total area of 122,738 m^2. In contrast to B1, this feature is characterized as a single landslide without any nested features (e.g., gullies). Visual analysis of satellite imagery shows that detectable slope movement began around the year 2000, which is consistent with the onset of accelerated lowering of the glacier surface in this region and accompanying debuttressing of ice-marginal topography. We selected 33 tie points evenly distributed in the B2 landslide area on the four-year UAV images (2016-2019) to monitor its surface displacement, which revealed that the landslide has moved by an average of 2.63±0.04 m a^{-1} in the UAV monitoring period, and the affected area has increased by 7,414m^2 via headscarp erosion. The highest rate of displacement was 4.32 cm d^{-1} and occurred between 2017-2018. Between 2011 and 2019, the collapsed area of B2 has expanded by 35,000 m^2, with an expansion rate of 4.99% a^{-1}. The landslide has a vertical glide distance of 48 m, and a horizontal displacement of 70 m. In the period 2017-2018 landslide activity forced the closure of a zigzag trail path (Fig. 5e) which was used for accessing the glacier.

Across the valley from B2, we identify landslide B3 (3100 m a.s.l, Fig. 5f, Fig. 6c), which is 805 m in length, 132 in width, and 63,241 m^2 in area and, like B2, is located on a lateral moraine close to the glacier terminus. The landslide has been effectively divided into five zones, delineated by four gullies (Fig. 5f). Analysis of satellite imagery shows that the landslide began to develop around 2013 when a headscarp is first detectable. Feature tracking (33 tie points) analysis on repeat UAV images shows that the landslide has moved down with an average rate of 1.65±0.04 cm d^{-1} between 2016 and 2019, with the highest rate of 1.97±0.04 cm d^{-1} occurring in the period 2017-2018.

Feature B4 (Fig. S2d) is also located on the north-facing (true right) lateral moraine slope of the glacier, approximately 3.5 km from the base of the icefall. It is ~103 m in height, 993 m in length, and covers an area of 73,270 m^2. Geomorphologically, this feature is the most complex of the type B PSFs, in that it represents a transition slope that it exhibits landslides in two distinct zones at either end (covering an area of 18,244 m^2, or 24.90% of the sediment-mantled moraine slope in this area) and also exhibits gully headward erosion (i.e., PSF Type C). Feature tracking analysis of 37 tie points indicates that the landslide moved

downslope at an average rate of 1.66±0.04 cm d^{-1} between 2016 and 2019, with a maximum rate of 2.63±0.04 cm d^{-1} in 2017-2018.

4.2.3 Gully headward erosion (PSF type C)

The three major paraglacial gully headward erosion areas (C1-C3, Fig. 5a) are located at the intersections between three tributary streams which are fed by seasonal snowmelt and the main trunk of the HLG ice tongue. They have a total area of ~324,000 m² in 2019. The UAV images did not cover the entire areas of Type C slopes, therefore we used five PL, RapidEye, and Google Earth images from 2002, 2011-2019 to supplement these data and monitor the development of these features (Fig. S8). Our mapping results show that the total area of these three gullies has expanded by ~93,000 m² between 2011 and 2019, with an annual expansion rate of 5.02% a^{-1}.

C1 is located on the northern slope of HLG at an altitude of 3200 m (Fig. 5g; Fig. S8a). In 2019 it had a length of 849 m, a width of 312 m and, an area of 139,135 m². It is adjacent to a major tributary stream that drains the northern side of the valley, and which intersects (and bisects) the true left lateral moraine where the glacier turns to flow eastward to its terminus. Field inspection of exposed surfaces at C1 reveals that it comprises a block of thick debris and sand deposits with some finer material, which was previously colonized by vegetation before being denuded by flowing water. In the period 2011-2015, the area of the gully expanded upslope at a rate of 10.44 m a^{-1}, and by 2019 the location of headward erosion was more clearly concentrated in the meltwater tributary channel (Fig. S8a). Between 2011 and 2019, the average upward denudation rate of the feature was 3.39 cm d^{-1} (12.20 m a^{-1}) and the exposed area had increased by 45,449 m² or 48.59% from 2011 (Tab. 2).

Gully C2 is situated on the southern slope (true right lateral moraine) of HLG at about 3200 m a.s.l (Fig. 5h; Fig. S8b) and in 2019 extended ~160 m in width, ~270 m in length, and 24,248 m^2 in area. The exposed area of the gully expanded upslope along the path of a meltwater-fed tributary stream, with a gradient of ~36° close to the HLG moraine, and which originates from Hailuogou No. 3 Glacier (29° 32.41’ N, 101 58.05’ E). This tributary stream connects directly to the subglacial water system of HLG. The gully is most actively eroding upstream of the point at which it connects to HLG, with an average upward denudation rate of 0.76 cm d^{-1} between 2002 and 2019, producing an increase in the exposed area of 11,923 m² in the same period.

Gully C3 is also located on the southern slope of HLG at 3500 m a.s.l (Fig. 5i; Fig. S8c), around ~800 m west of gully C2. The gully is formed by a tributary stream which is fed by meltwater from Hailuogou No. 2 Glacier (29° 32.82’ N, 101° 56.92’ E), which became detached from HLG sometime after the 1930s (Liu and Zhang, 2017) and has since retreated to the edge of ice scarped ridge. The gully is filled with glaciofluvial sediment and is deeply incised. Like C2, meltwater also flows into HLG glacier subglacially. Since 2002, expansion of the sediment-mantled area of this gully has occurred on the right (east) side of the gully and has recently begun to expand up along the left (west) bank of the channel. We expand the area of the gully to

incorporate adjacent unvegetated lateral moraine, which also shows evidence of gullying and headward erosion. The total area of C3 increased by 14.3%, from 109,500 m^2 in 2002 to 160,474 m^2 in 2019.

5 Discussion

5.1 Possible forcing mechanism of the three types PSFs in HLG

Many potential factors, include glacial history (mostly downwasting or debuttressing in HLG since Little Ice Age), rock structure (i.e., joint), seismicity, and meteorological disturbances (i.e., precipitation, temperature, and freeze-thaw cycling), have been generally considered as preconditioning, preparatory or triggering factors that combine to produce a PSF (McColl, 2012). In the discussion below we refer to these factors to discuss their relative importance in forcing the different types of PSF that we observed at the HLG.

5.1.1 Rockfall

Small-scale rockfalls are commonly found sourcing from exposed bedrock walls on both sides of the HLG ice tongue. These exposed bedrock walls are generally granite rocks characterised by well-developed vertical joints (Fig. S6 and S7), which make the slope more prone to failure or more likely failure under given triggers (Draebing and Krautblatter, 2019). In addition to glacier erosional steepening (Herman et al., 2021), the exposure of these bedrocks can also accelerate the weathering process and rock strength degradation (Matsuoka, 2008). Intensification of freeze-thaw conditions during deglaciation may have led to more enhanced rockfall activity since winter seasons in the HLG environment is cold enough to cause frozen water within rock fractures and pore spaces. During monsoon seasons, the warm humid environment can also be a stimulative factor leading to intense and rapid chemical weathering of the exposed rock wall (Li et al., 2019). However, the frequency and magnitude dynamics of these small-scale rockfalls are difficult to be determined by this study since their specific occurring time was unknown and many formal rockfalls may be overlapped by later ones during our investigation period. In the following part of this section, we will focus on discussing possible forcing mechanisms of a larger-scale rockfall event that occurred in 2018, which we could confirm its occurring time (around 15 Oct. 2018) and estimate its magnitude from UAV surveys.

The 2018 rockfall (Fig. 5b) represents a rapid non-ice contact rock collapse adjacent to an area of the glacier that has experienced remarkable (80-100 m) thinning since its Little Ice Age (LIA) maximum (Fig. 5c). More widely in the Mt. Gongga region, glacial and paraglacial landform assemblages display a strong influence of Late Pleistocene and Holocene glaciations, the most striking example of which are the deeply incised trunk and tributary valleys formed by higher rates of glacier erosion (Liu et al., 2009), glaciofluvial activity, and monsoonal precipitation; as such, paraglacial slopes are strongly modified by local glacial history, making this an important preconditioning and preparatory factor for rockfall. Anecdotally, small-scale rock collapses occur all year round on both sides of HLG (Fig. 5a; Fig. S7), especially from those rock slopes exhibiting vertical jointing. Our field investigations indicate that the main detachment zone of the 2018 rockfall has no faults but is highly jointed,

which facilitates liquid water ingress and hydraulic erosion and is also conducive to promoting fracturing via freeze-thaw and ice segregation processes (Rodríguez-Rodríguez et al., 2018) which gradually loosens the rock block and might also be considered a trigger in causing blocks to eventually break away from the rock valley walls (Fischer et al., 2010).

The annual mean temperature was relatively low in 2018 (4.5°C) compared to the preceding four years (5.0°C, Fig. 6a). Fig. 6b shows the antecedent rainfall in the five to ten days before the rockfall occurred (5-20 Oct 2018) and compares antecedent rainfall statistics between five years (2014-2018). The mean daily precipitation between 5 and 20 Oct 2018 is 5.89 mm which is significantly higher than in 2014, 2015, and 2017, although not significant compared with 2016, the value is still high. Additionally, the differences in the daily mean temperature between September to October 2018 and September to October 2014-2017 were relatively large (Fig. 6c; from September to October 2018, a large amount of daily temperature data was missing from the automatic observation and was therefore offset by manual observations (MO), as mentioned in subsection 3.4 above); the daily mean temperature was between 0.4 to 5.3°C from 01 to 09 October 2018 compared to a range of 3.6-12.92°C for the preceding four years. From 20 to 29 September, the mean daily temperature was similar to the preceding four years with a range of 6.6-13.3°C. The temperature lapse rate (0.0065°C m^{-1} in humid air, (Hemond and Fechner, 2015)) have shown that when the temperature at the Gongga Mt. Station (3000 m a.s.l.) drops to about 6°C, the temperature on the mountain at 4000 m a.s.l. approaches 0°C and freezing of water begins. We, therefore, speculate that the abundant precipitation in the early days caused a large amount of liquid water to ingress the rock fissure, then the frost heave caused the rock mass to eventually rupture (e.g. (Hartmeyer et al., 2020)). We finally suggest that abnormal precipitation and low temperature in 2018 may have acted as a preparatory factor and triggering factor for the observed rockfall, respectively.

Rockfall and other mass movements can be triggered by seismic activity, which can also act as a preparatory factor through its ability to cause rock damage (Huggel et al., 2007). The HLG region is seismically active, and in the last five years has recorded 9 seismic events ranging from 2.9-3.8 in magnitude, all of which occurred in the period 2016-2017 (China Earthquake Administration, *https://www.cea.gov.cn/*). Although no significant seismic events were observed immediately prior to the 2018 rockfall, rock mass damage associated with the historical seismic activity may have acted as a preparatory factor for the 2018 rockfall and other mass movements from deglaciated slopes in the wider catchment.

5.1.2 Sediment-mantled slopes slide

Type B PSFs are largely associated with lateral moraine instability and collapse. Elsewhere (north-facing slopes, Fig. S9) in the catchment we observe glacially smoothed and polished bedrock surfaces with steep inclination angles (a product of the geological, glacial, and climatic history of the catchment), and we infer that the failure of these unconsolidated slopes is caused by glacier downwasting and debuttressing (Cody et al., 2020), combined with a material angle of repose which is lower than the inclination of the underlying bedrock surface; sediment-mantled slopes showing evidence of instability typically have a slope angle of ~29°, whilst the inclination of exposed bedrock slopes close to the elevation of the present-day glacier surface

is ~45°. Whilst historically the glacier has essentially 'propped up' the lateral moraines, rapid reduction in the elevation of the glacier surface has directly contributed to slope instability, which is increasing in speed, corresponding to findings in van Woerkom et al. (2019).

Debris flow may also be a preparatory factor causing slope instability. A gully developing process was observed within Type B failures (as mentioned in subsection 4.2.2 above). Based on 17 years (2002-2019) RS monitoring of the B3 slope (Fig. S10), for example, we found that the surficial debris flow occurred before the hillslope movement. Firstly, some debris flows occurred, forming 3 gullies, and no slide was evident in 2002. Secondly, the debris flow gullies gradually expanded, the number increased to 5, the slope slid slightly, and the slide cracks were starting to form around in 2013. Finally, the debris flow gullies increased to 6 and expanded further (the largest gully is about 130 m wide at its widest point), the slope slide significantly (up to 2 cm d^{-1} between 2017 and 2018; Fig. S2), and the cracks increased in response to rapid glacier downwasting in 2019, which is different from the discovery of the Fox glacier in New Zealand by Cody et al. (2020).

The regional and local climate, which is characterized by abundant precipitation during the monsoon season, enables rapid succession of vegetation on deglaciated slopes. However, although this vegetation is extensive in its coverage, particularly on slopes immediately above the lateral moraines, it mostly comprises species with a shallow rooting depth that do not have a strong capacity to increase slope stability, especially at larger scales; shrub vegetation growing on the unstable B2 and B3 slopes are relatively young and do not mitigate deep translational failure, whereby unconsolidated sediment slides along the interface between the overlying moraine and steep underlying bedrock. We also observed that the displacement of all type B PSFs reached their maximum rate during the period 2017-2018, and upper parts of the slope failures speed up to the same extent as the lower parts (Fig. S3), which may in part be related to increased air temperature (promoting enhanced glacier downwasting) and precipitation extremes in 2018.

5.1.3 Gully headward erosion

Glacier downwasting and meltwater from deglaciating tributary catchments enhance erosion of ice-marginal gullies and contribute to the expansion of actively eroding slopes in these landscapes; headward erosion of sidewall tributary gullies occurs as the local base level (i.e., the HLG glacier surface) falls (Williams and Koppes, 2020;Schiefer and Gilbert, 2007), and this effect is illustrated clearly at PSF C1 (Fig. 5g).

The upstream sediments were transported and accumulated along the gullies to both sides of the glacier, with a fast erosion rate, for instance, the part with the largest change in C1 area moved about 150 m in both horizontal and vertical directions. Therefore, we argue that surface fluvial erosion and glacier debuttressing simultaneously trigger the instability of the type C slopes (Dusik et al., 2019).

All the three major type C slopes are developed along the tributary streams, in which settings slope slides are usually limited but surface fluvial erosion plays the primary role. There should exist a seasonal plus or enhanced headward erosion rates, i.e., during the monsoon rainstorm seasons. However, we still could not track this process due to the lack of higher resolution observations in the current study. Nevertheless, it is suggested that this type of paraglacial adjustment is still in active process based on the currently observed situation at both lateral sides of the HLG. As the increase of the exposed area and the erosionable baseline, a period of accelerated sediment/debris flux to the surface or base of the glacier is expected in the following years.

5.2 Paraglacial geomorphology process in deglaciating monsoonal temperate environments

Meteorological observations at the Gongga Mountain Station (Fig.1) show that the regional mean annual temperature has increased by >1 °C and annual precipitation has decreased at a rate of 9.13 mm a^{-1} over the past 30 years (Fig. 6a). Warming and a weakened monsoon, as also occurred at other parts of the SETP (Yao et al., 2012), have induced recent remarkable downwasting of HLG and serves as a preparatory or triggering factor for PSFs. Our case study at the HLG has demonstrated that paraglacial slopes in the deglaciating monsoon temperate environment are characterised by the geomorphology process with multi types, fast responding, and a high rate of denudation. In Mt. Gongga and most SETP monsoon dominate regions, a climate of warm-wet synchronization is the primary precondition driving the physical or hydrothermal dynamics of both glacier and off-glacier processes.

5.2.1 Impact of the monsoonal climatic conditions

Climatic conditions (e.g., seasonal distribution and multi-year fluctuation of temperature and precipitation) can directly affect slope stability (McColl, 2012;Coe, 2020). Climate at the HLG is strongly affected by the southeast monsoon (An et al., 2015;Lau and Yang, 1997) characterised by a warm and wet summer and relative colder and drier winter (Liu et al., 2010). According to the observation of Gongga station at 3000 m a.s.l. during the period 1988-2018, the mean annual temperature near the HLG was 4.5 ℃, but the recorded highest summer temperature was 27 ℃ in 2010 and the lowest winter temperature was -16.8 ℃ in 2016 (Fig. 6d). The mean annual maximum temperature range between 1988 and 2018 was close to 40℃, with a slightly increasing trend since 2001 (Fig. 6d). This large diurnal (Fig. 6c) and annual (Fig. 6a) variation of temperature at the HLG could affect the slope freeze-thaw process and destabilize paraglacial slopes through thermodynamics (Fischer et al., 2012;Curry et al., 2006).

The rain gauge recorded an average annual number of 314 days and a mean annual amount of 1912 mm precipitation, of which 88% amount was concentrated in ablation seasons (April to October) and ~42% was concentrated in summer (July to September). Abundant rainfall in the monsoon area results in the absolute high-amount precipitation in Mt. Gongga has further promoted the instability of slopes. Due to frequent summer rainstorms, small-scale debris flows are commonly found in both lateral sides of the HLG valley. These tributary flash floods or small-scale debris flows sometimes flow over/through the

destabilized lateral moraine, furtherly disturbing the slopes and promoting the slide. The occurrence of nested processes in Type B (Fig. 5f, S8b, and S11) is similar to that debris flow galleys observed at lower moraine slips reported by Cody et al. (2020) at paraglacial slopes in South Alps temperate glaciers, where the local annual precipitation is observed several times higher than our study area (Kerr et al., 2018). In addition, the combination of extreme temperature and precipitation conditions can also trigger slope instability (as mentioned in subsection 5.1.1 above - the relatively low temperature and high precipitation in 2018 may be the cause of rockfall).

5.2.2 Interaction between paraglacial slope process and dynamics of a temperate glacier

Temperate glaciers in monsoon conditions generally show more remarkable and fast response to the change of temperature and precipitation than cold glaciers (He et al., 2003;Su and Shi, 2002), characterised by high mass turnover and fast flow rate (Oerlemans, 1997), and developed en- and sub-glacial drainage systems (Fountain and Walder, 1998). Glacier downwasting can trigger the failure of Type B and C (as mentioned in subsection 5.1.2 and 5.1.3 above). According to Fig. 3 and 4, in profile D-D', the D' side has been thinned (with a mean rate of -1.0 m a^{-1}) and slowed (the mean daily velocity changed by -0.27 m d^{-1}) more significantly than that on the D side (with a mean rate of 0 m a^{-1} and the mean daily velocity changed by -0.14 m d^{-1}, respectively) in the latest study period, resulting in the slope failure on D' side has been faster. The exposed slopes may increase the absorption of long-wave thermal radiation on the surface, contributing to the melting of glaciers in nearby areas. Profile E-E' showed uniform thinning in both two periods (Fig. 3b, -1.0 m a^{-1}), caused the landslides to appear on both sides. For both profiles B-B' and C-C', the thinning rate changed from ~0 m a^{-1} in 1966-2000 to ~-2 m a^{-1} in 2000-2016 (Fig. 3b), which may be related to the inner stress adjustment in the glacier - the ice mass of upstream replenishment the acceleration loss of downstream. Both sides of the profile B-B' are mainly steep bedrock, with a limited accumulation of lateral moraine materials, such that type A is the dominant PSF. The glacier downwasting is mainly used as a preparatory factor for the slope instability, here. The relationship between climatic change, glacier downwasting, and PSF can be shown in Fig. 7.

Despite a slowdown in recent decades (Fig. 3c), the flow velocity of HLG is still higher than most mountain glaciers in Himalaya, Tian Shan, and inner Tibet (Bhushan et al., 2018;Wang et al., 2016;Zhang et al., 2010;Ke et al., 2013). Previous work has quantified the evolution of the glacier's subglacial and englacial hydrology, and revealed a highly efficient hydrological system that is maintained in both summer and winter months (Liu and Liu, 2010); an abundance of meltwater and subglacial and englacial debris (which we infer because of the debris-covered nature of the glacier, e.g. (Miles et al., 2021)) act as effective "grinding tools" for glacial abrasion. The estimated erosion rate is 2.2-11.4 mm a^{-1} (Based on the current glacier thickness and flow velocity, a conservative estimate of the glacier bedrock erosion depth is about 1-5 m) which is consistent with other temperate glaciers but higher than the continental glaciers (0.1-1.0 mm a^{-1})(Liu et al., 2009). A high erosion rate contributes to valley incision and the steepening of valley flanks, which increase in exposed area and angle and therefore likely to become more prone to instability.

The intense mass flux due to PSFs, on the other hand, can deliver abundant debris materials to the glacier system. According to Fig 4b, the PBGA was equivalent to ~11% of the GCA in 1990 and increased to ~69% in 2020, providing an ample source of sediment for the glacial environment. For instance, there is much debris that fell onto the glacier surface from rockfalls and debris slide/flow process. We calculated the total areal of all observed rockfalls covered 62216 m^2 (volume class: 10^4~10^5 m^3); according to Scherler et al., (2018) the supraglacial debris cover of HLG is 2.71 km^2, as a result, the total areal contributions to supraglacial debris-cover of the rockfalls is 2.3%. Due to the high supraglacial debris-cover of HLG (11 %), the contribution rate of rockfalls observed in this study is lower than that of the European Alps and the Southern Alps of New Zealand rockfalls of the same class (Fischer et al., 2012). We also observed a limited number of materials that are delivered to the supraglacial environment through direct roll (Fig. S11 (a); the sediments are more dispersed compared to rockfalls), collapse (Fig. S11 (b)), and debris flow (Fig. S11 (c); faster changes). Among them, two collapsed parts of the B2 slope were quantified by using UAV imagery in the 718 days from 2016/8/31 to 2018/8/19, the collapsed area increased by 94% in total, with an increased rate of 8 m^2 d^{-1}. These sediment delivery process increasing the range and thickness of the supraglacial debris-cover, which in turn affected the surface energy balance for melting and therefore downwasting rate of the glacier, which will thus influence the rate of runoff generation and its contribution to the sea level rise from glacierised catchments. Additionally, some processes (e.g., Type C slopes) can also deliver materials to the sub-glacial environment through runoff (Fig. S11 (d)). Their contribution to glacial sediments is hard to quantify, but it is clear that this process does result in a long-term and steady sediments supply to the glacier.

Finally, failing rock debris may sink into the glacier if the stress they exert exceeds the resistance provided by the glacier ice since rock is higher in density than ice. This geomorphological phenomenon has been identified in the Southern Alps of New Zealand (McColl and Davies, 2013), where mountain glaciers occupy equally steep valleys. Field evidence from the monitoring of the B2 slope by UAV images for four consecutive years (Fig S6b) indicates that the glacier in this vicinity has narrowed or squeezed. The direction of the glacier movement at the boundary with B2 changes as B2 advances, which causes the original arc of the glacier boundary to be destroyed. The greatest change in the location of the glacier boundary bordering slope B2 is during the period 2017-2018, which is consistent with the fastest displacement speed (~4.32 cm d^{-1}) of the slope during the wider monitoring campaign. Our results may imply that the weight of the moraine may be sufficient to deform the glacier ice, as hypothesized by McColl and Davies (2013).

5.2.3 Other geomorphological and environmental implications

Similar to other studies (Dunning et al., 2015;Glueer et al., 2020;Hedding et al., 2020), our analyses show a temporal and spatial component to PSF development following rapid deglaciation of the HLG. Following many thousands of annual thermo-hydromechanical loading cycles, which promote rock damage (Grämiger et al., 2017;Glueer et al., 2020) the bedrock slopes bordering HLG are well-prepared for failure, and this response is beginning to manifest as specific triggering events occur and/or mechanical rock mass thresholds are crossed. Similarly, unconsolidated lateral moraines show signs of increasing

deformation and translational movement in response to glacier downwasting and debuttressing; we hypothesize that this will continue until critical angles of repose are reached, which will be followed by vegetation colonisation and soil development (Eichel et al., 2018).

With respect to the terrain aspect, we found that south-facing slopes show more instabilities, both in terms of magnitude and frequency. Firstly, it could be related to the differences in the availability of material (Fig. S9; i.e. asymmetrical deposition of glacial drift and moraine construction on either side of the valley), with more sediment on the south-facing slopes and slope angles (Fig. S9). Secondly, it could also be related to the differences in glacier surface altitude and ice thinning rate, which is particularly obvious compared to the C-C', D-D', and E-E' profiles. It can be seen from profile D-D' in Fig. 3 a, b that the altitude and thinning rate of the glacier under the south-facing slope are much greater than that on the opposite side (ice thinning rate of difference was 1.5 m a^{-1}), which may be caused by the lower surface temperature due to the topographic shading on the glacier areas under the north-facing slope (Liao et al., 2020). Therefore, PSFs and glaciers downwasting show the same temporal and spatial movement. This observed pattern further indicates that there is a direct connection between glacier downwasting and PSFs occurrence. Additionally, unstable slopes are more likely to occur in areas with lower surface gradients (all-around 30°, as mentioned in subsection 4.2 above) is contrary to the general conclusion of the many landslides study - the steeper the slope, the stronger the shear stress and the lower the factor of safety (McColl, 2015), which may be related to the slope material or the slope adjustment after failure process.

Based on the above analysis, we suggest a conjectural paraglacial slope evolution and slope sediment delivery model of HLG (Fig. 8). After the glacier was downwasting from the initial state (Stage I), the upper part of the steep moraine slope quickly destabilized, making the entire slope slow sliding, corresponding to those findings by van Woerkom et al. (2019), Ballantyne (2013), and Cully et al. (2006); then the moraine slope slowly slides down (Stage II; which were observed in Type B and part of Type C) and some part of them is exfoliated with underneath bedrock exposed. During the exposure of moraine, vegetation may be colonized, or gullies may be formed by debris (or water) flows washing away (stage II a); when the gullies gradually expand, headward erosion may occur in the upper of the gullies (Stage II b; which were observed in Type C). Sediments at the base of the slope or fell onto the glacier surface are transferred again as the glacier moves (Stage III); until the slope is steepest (>50°) when moraine has been removed and bedrock is completely exposed to the ground and may collapse through some disturbances, finally (Stage IV; Type A).

6 Conclusion

We used repeat mappings by UAV and satellite remote sensing as the basis for identifying and analysing the evolution of three styles of PSF at HLG between 1990 and 2020 and explore these results in the context of their potential driving mechanisms. Over the investigation period, the glacier terminus has retreated ~510 m (17 m a^{-1}), its surface has down-wasted by -0.88 m a^{-}

^{1}, with thinning observed over 83.50% of the ablation zone study area, and the glacier velocity has slowed from a mean of 0.32 m d^{-1} (period 1982 to 1983) to 0.11 m d^{-1} (2014 to 2018). Rapid downwasting of the glacier surface has exposed oversteepened ice-marginal slope topography, which shows evidence of the overall PBGA increased from 0.31±0.27 km^2 in 1990 to 1.38±0.06 km^2 in 2020; and of widespread instability in the form of (A) rockfall from bedrock slopes, (B) slide of unconsolidated lateral moraines, and (C) increased erosion activity in tributary valleys, with a total area of 0.74±0.03 km^2 in 2020. South-facing valley slopes (true left of the glacier) exhibited more destabilization (56% of the total PSFs area) than north-facing (true right) valley slopes (44% of the total PSFs area). Set against a background of frequent, small-scale rockfalls that are anecdotally recorded in the area, a large rockfall occurred in Autumn 2018. Non-ice-contact rockfalls in deglaciating catchments are a well-established, short- to long-term response of paraglacial slopes following glacier downwasting and rock slope exposure, however, analysis of antecedent meteorological conditions suggests that abundant precipitation and low temperature may have served to prepare, and perhaps trigger this rock slope failure. Deformation of sediment-mantled moraine slopes (mean 1.6-2.6±0.04 cm d^{-1}) and an increase in erosion activity in ice-marginal tributary valleys caused by a drop in local base level (gully headward erosion rates are 0.7-3.39 cm d^{-1}) have occurred in tandem with recent glacier downwasting. The PSFs and even the whole PBGA providing an ample source of sediment for the glacial environment. At the base of the analysis of paraglacial slope evolution and slope sediment delivery, we speculated that the occurrence of some unstable slopes in the lower slope angle areas may be related to the slope material and the failure process. In general, the formation, evolution, and current status of these typical PSFs are generally related to the history of glacier dynamics and paraglacial geomorphological adjustments, and also influenced and/or disturbed by the fluctuation of air temperature/precipitation and their combinations. Longer-term monitoring will provide a clearer picture of the feedbacks between (accelerating) glacier downwasting, climatic conditions, and paraglacial landscape response in this data-poor region.

Data availability

The paraglacial slope failure shape files can be requested by email from the first author zhongyan19@mails.ucas.ac.cn

Author contributions

QL and XL initiated the underlying research project and obtained the funding. QL developed the research goal and designed the study. QL, YN, BZ, JC, HL and GL performed the primary UAV data. QL and YZ conducted and analysed the data. YZ, QL, MW, YN and FP wrote the paper.

Competing interests

The authors declare that they have no conflict of interest.

Acknowledgements

This work was funded by the NSFC Project (41871069) and the Sichuan Science and Technology Programs (2021JDJQ0009, 2020JDJQ0002). The authors gratefully acknowledge the PlanetLab for provision of PlanetScope and RapidEye imagery, and U.S. Geological Survey for Landsat satellite images. MW and FP acknowledge funding from Royal Society-Newton Fund project 'Understanding glacier and hydrological changes in the Tibetan Plateau using high-resolution monitoring and modelling'.

References

An, Z., Wu, G., Li, J., Sun, Y., Liu, Y., Zhou, W., Cai, Y., Duan, A., Li, L., Mao, J., Cheng, H., Shi, Z., Tan, L., Yan, H., Ao, H., Chang, H., and Feng, J.: Global Monsoon Dynamics and Climate Change, Annual Review of Earth and Planetary Sciences, 43, 1-49, 10.1146/annurev-earth-060313-054623, 2015.

Ballantyne, C.: Paraglacial landsystems, Glacial Landsystems. Arnold, London, 432, 461, 2003.

Ballantyne, C. K., and Benn, D. I.: Paraglacial Slope Adjustment and Resedlmenfation following Recent Glacier Retreat, Fåbergstølsdalen, Norway, Arctic and Alpine Research, 26, 255-269, 10.1080/00040851.1994.12003065, 1994.

Ballantyne, C. K.: Paraglacial geomorphology, Quaternary Science Reviews, 21, 1935-2017, doi:10.1016/S0277-3791(02)00005-7, 2002.

Ballantyne, C. K.: PERMAFROST AND PERIGLACIAL FEATURES | Paraglacial Geomorphology, in: Encyclopedia of Quaternary Science (Second Edition), edited by: Elias, S. A., and Mock, C. J., Elsevier, Amsterdam, 553-565, 2013.

Ballantyne, C. K., Wilson, P., Gheorghiu, D., and Rodés, À.: Enhanced rock-slope failure following ice-sheet deglaciation: timing and causes, earth surface processes and landforms, 39, 900-913, doi:10.1002/ESP.3495, 2014.

Bhushan, S., Syed, T. H., Arendt, A. A., Kulkarni, A. V., and Sinha, D.: Assessing controls on mass budget and surface velocity variations of glaciers in Western Himalaya, Scientific Reports, 8, 8885, doi:10.1038/s41598-018-27014-y, 2018.

Brun, F., Berthier, E., Wagnon, P., Kääb, A., and Treichler, D.: A spatially resolved estimate of High Mountain Asia glacier mass balances from 2000 to 2016, Nature Geoscience, 10, 668-673, doi:10.1038/ngeo2999, 2017.

Cai, J., Jia, H., Liu, G., Zhang, B., Liu, Q., Fu, Y., Wang, X., and Zhang, R.: An Accurate Geocoding Method for GB-SAR Images Based on Solution Space Search and Its Application in Landslide Monitoring, Remote Sensing, 13, 832, doi:10.3390/rs13050832, 2021.

Cao, B., Pan, B., Guan, W., Wen, Z., and Wang, J.: Changes in glacier volume on Mt. Gongga, southeastern Tibetan Plateau, based on the analysis of multi-temporal DEMs from 1966 to 2015, Journal of Glaciology, 65, 366-375, 2019.

Chen, C., Zhang, L. M., Xiao, T., and He, J.: Barrier lake bursting and flood routing in the Yarlung Tsangpo Grand Canyon in October 2018, journal of hydrology, 583, doi:10.1016/J.JHYDROL.2020.124603, 2020.

Cheng, Z. L., Liu, J. J., and Liu, J. K.: Debris flow induced by glacial lake break in southeast Tibet, wit transactions on engineering sciences, 67, 101-111, doi:10.2495/DEB100091, 2010.

Church, M., and Ryder, J. M.: Paraglacial Sedimentation: A Consideration of Fluvial Processes Conditioned by Glaciation, GSA Bulletin, 83, 3059-3072, doi:10.1130/0016-7606(1972)83[3059:psacof]2.0.co;2, 1972.

Cody, E., Anderson, B. M., McColl, S. T., Fuller, I. C., and Purdie, H. L.: Paraglacial adjustment of sediment slopes during and immediately after glacial debuttressing, Geomorphology, 371, 107411, doi:10.1016/j.geomorph.2020.107411, 2020.

Coe, J. A.: Bellwether sites for evaluating changes in landslide frequency and magnitude in cryospheric mountainous terrain: a call for systematic, long-term observations to decipher the impact of climate change, Landslides, 17, 2483-2501, doi:10.1007/s10346-020-01462-y, 2020.

Cook, S. J., Porter, P. R., and Bendall, C. A.: Geomorphological consequences of a glacier advance across a paraglacial rock avalanche deposit, Geomorphology, 189, 109-120, doi:10.1016/j.geomorph.2013.01.022, 2013.

Curry, A. M., Cleasby, V., and Zukowskyj, P.: Paraglacial response of steep, sediment-mantled slopes to post-'Little Ice Age' glacier recession in the central Swiss Alps, Journal of Quaternary Science, 21, 211-225, 10.1002/jqs.954, 2006.

Deline, P., Gruber, S., Delaloye, R., Fischer, L., Geertsema, M., Giardino, M., Hasler, A., Kirkbride, M., Krautblatter, M., and

Magnin, F.: Ice loss and slope stability in high-mountain regions, in: Snow and Ice-related hazards, risks and disasters, Elsevier, 521-561, 2015a.
Deline, P., Hewitt, K., Reznichenko, N., and Shugar, D.: Chapter 9 - Rock Avalanches onto Glaciers, in: Landslide Hazards, Risks and Disasters, edited by: Shroder, J. F., and Davies, T., Academic Press, Boston, 263-319, 2015b.
Draebing, D., and Krautblatter, M.: The Efficacy of Frost Weathering Processes in Alpine Rockwalls, Geophysical Research Letters, 46, 6516-6524, doi:10.1029/2019GL081981, 2019.
Dunning, S. A., Rosser, N. J., McColl, S. T., and Reznichenko, N. V.: Rapid sequestration of rock avalanche deposits within glaciers, Nat Commun, 6, 7964, doi:10.1038/ncomms8964, 2015.
Dusik, J.-M., Neugirg, F., and Haas, F.: Slope Wash, Gully Erosion and Debris Flows on Lateral Moraines in the Upper Kaunertal, Austria, in: Geomorphology of Proglacial Systems: Landform and Sediment Dynamics in Recently Deglaciated Alpine Landscapes, edited by: Heckmann, T., and Morche, D., Springer International Publishing, Cham, 177-196, 2019.
Eichel, J., Krautblatter, M., Schmidtlein, S., and Dikau, R.: Biogeomorphic interactions in the Turtmann glacier forefield, Switzerland, Geomorphology, 201, 98-110, doi:10.1016/j.geomorph.2013.06.012, 2013.
Eichel, J., Draebing, D., and Meyer, N.: From active to stable: Paraglacial transition of Alpine lateral moraine slopes, Land Degradation & Development, 29, 4158-4172, 10.1002/ldr.3140, 2018.
Emmer, A., Klimeš, J., Hölbling, D., Abad, L., Draebing, D., Skalák, P., Štěpánek, P., and Zahradníček, P.: Distinct types of landslides in moraines associated with the post-LIA glacier thinning: Observations from the Kinzl Glacier, Huascarán, Peru, Science of The Total Environment, 739, 139997, doi:10.1016/j.scitotenv.2020.139997, 2020.
Fan, J., An, C., Zhang, X., Li, X., and Tan, J.: Hazard assessment of glacial lake outburst floods in Southeast Tibet based on RS and GIS technologies, International Journal of Remote Sensing, 40, 4955-4979, doi:10.1080/01431161.2019.1577578, 2019.
Farr, T. G., Rosen, P. A., Caro, E., Crippen, R., Duren, R., Hensley, S., Kobrick, M., Paller, M., Rodriguez, E., Roth, L., Seal, D., Shaffer, S., Shimada, J., Umland, J., Werner, M., Oskin, M., Burbank, D., and Alsdorf, D.: The Shuttle Radar Topography Mission, Reviews of Geophysics, 45, doi:10.1029/2005RG000183, 2007.
Fickert, T., and Grüninger, F.: High-speed colonization of bare ground—Permanent plot studies on primary succession of plants in recently deglaciated glacier forelands, Land Degradation & Development, 29, 2668-2680, doi:10.1002/ldr.3063, 2018.
Fischer, L., Amann, F., Moore, J. R., and Huggel, C.: Assessment of periglacial slope stability for the 1988 Tschierva rock avalanche (Piz Morteratsch, Switzerland), Engineering Geology, 116, 32-43, doi:10.1016/j.enggeo.2010.07.005, 2010.
Fischer, L., Purves, R. S., Huggel, C., Noetzli, J., and Haeberli, W.: On the influence of topographic, geological and cryospheric factors on rock avalanches and rockfalls in high-mountain areas, Nat. Hazards Earth Syst. Sci., 12, 241-254, 10.5194/nhess-12-241-2012, 2012.
Fountain, A. G., and Walder, J. S.: Water flow through temperate glaciers, Reviews of Geophysics, 36, 299-328, 1998.
Fyffe, C. L., Woodget, A. S., Kirkbride, M. P., Deline, P., Westoby, M. J., and Brock, B. W.: Processes at the margins of supraglacial debris cover: Quantifying dirty ice ablation and debris redistribution, Earth Surface Processes and Landforms, 45, 2272-2290, doi:10.1002/esp.4879, 2020.
Glueer, F., Loew, S., and Manconi, A.: Paraglacial history and structure of the Moosfluh Landslide (1850–2016), Switzerland, Geomorphology, 355, 106677, doi:10.1016/j.geomorph.2019.02.021, 2020.
Grämiger, L. M., Moore, J. R., Gischig, V. S., Ivy-Ochs, S., and Loew, S.: Beyond debuttressing: Mechanics of paraglacial rock slope damage during repeat glacial cycles, Journal of Geophysical Research: Earth Surface, 122, 1004-1036, doi:10.1002/2016JF003967, 2017.
Haiguanju: Hailuogou Scenic Area achieved another record in tourist reception in 2019, http://www.gzz.gov.cn/gzzrmzf/c100044/202001/38048f67a8d3431fa8fe98d250b42281.shtml, 2020.
Haritashya, U. K., Kargel, J. S., Shugar, D. H., Leonard, G. J., Strattman, K., Watson, C. S., Shean, D., Harrison, S., Mandli, K. T., and Regmi, D.: Evolution and Controls of Large Glacial Lakes in the Nepal Himalaya, remote sensing, 10, doi:10.3390/RS10050798, 2018.
Hartmeyer, I., Delleske, R., Keuschnig, M., Krautblatter, M., Lang, A., Schrott, L., and Otto, J. C.: Current glacier recession causes significant rockfall increase: the immediate paraglacial response of deglaciating cirque walls, Earth Surf. Dynam., 8, 729-751, doi:10.5194/esurf-8-729-2020, 2020.
He, Y., Zhang, Z., H.Theakstone, W., Chen, T., Yao, T., and Pang, H.: Changing features of the climate and glaciers in China's monsoonal temperate glacier region, Journal of Geophysical Research, 108, 4530-4536, 2003.

He, Y., Li, Z., Yang, X., Jia, W., He, X., Song, B., Zhang, N., and Liu, Q.: Changes of the Hailuogou Glacier, Mt. Gongga, China, against the background of global warming in the last several decades, Journal of China University of Geosciences, 19, 271-281, 2008.

Hedding, D. W., Erofeev, A. A., Hansen, C. D., Khon, A. V., and Abbasov, Z. R.: Geomorphological processes and landforms of glacier forelands in the upper Aktru River basin (Gornyi Altai), Russia: evidence for rapid recent retreat and paraglacial adjustment, Journal of Mountain Science, 17, 824-837, doi:10.1007/s11629-019-5845-5, 2020.

Hemond, H. F., and Fechner, E. J.: Chapter 4 - The Atmosphere, in: Chemical Fate and Transport in the Environment (Third Edition), edited by: Hemond, H. F., and Fechner, E. J., Academic Press, Boston, 311-454, 2015.

Hewitt, K., Clague, J., and Deline, P.: Catastrophic Rock Slope Failures and Mountain Glaciers, in: Encyclopedia of Snow, Ice and Glaciers, edited by: Singh, V, P., Singh, P, and Haritashya, Springer, pp. 113-126, 2011.

Hu, G., Chen, N., Deng, M., and Wang, Y.: Classification and Initiation Conditions of Debris Flows in Linzhi Area, Tibet, Bulletin of Soil and Water Conservation, 31, 193-197+221, 2011.

Huggel, C., Caplan-Auerbach, J., Waythomas, C. F., and Wessels, R. L.: Monitoring and modeling ice-rock avalanches from ice-capped volcanoes: A case study of frequent large avalanches on Iliamna Volcano, Alaska, Journal of Volcanology and Geothermal Research, 168, 114-136, doi:10.1016/j.jvolgeores.2007.08.009, 2007.

Hungr, O., Leroueil, S., and Picarelli, L.: The Varnes classification of landslide types, an update, Landslides, 11, 167-194, doi:10.1007/s10346-013-0436-y, 2014.

Jarman, D.: Large rock slope failures in the Highlands of Scotland: Characterisation, causes and spatial distribution, engineering geology, 83, 161-182, doi:10.1016/J.ENGGEO.2005.06.030, 2006.

Kääb, A., Jacquemart, M., Gilbert, A., Leinss, S., Girod, L., Huggel, C., Falaschi, D., Ugalde, F., Petrakov, D., Chernomorets, S., Dokukin, M., Paul, F., Gascoin, S., Berthier, E., and Kargel, J. S.: Sudden large-volume detachments of low-angle mountain glaciers – more frequent than thought?, the cryosphere, 15, 1751-1785, doi:10.5194/TC-15-1751-2021, 2021.

Ke, C.-Q., Kou, C., Ludwig, R., and Qin, X.: Glacier velocity measurements in the eastern Yigong Zangbo basin, Tibet, China, journal of glaciology, 59, 1060-1068, doi:10.3189/2013JOG12J234, 2013.

Kerr, T., Henderson, R., and Sood, A.: The precipitation distribution across Westland Tai Poutini National Park, Journal of Hydrology (NZ), 57, 1-23, 2018.

Kirkbride, M. P., and Deline, P.: Spatial heterogeneity in the paraglacial response to post-Little Ice Age deglaciation of four headwater cirques in the Western Alps, Land Degradation & Development, 29, 3127-3140, doi:10.1002/ldr.2975, 2018.

Korup, O., Montgomery, D. R., and Hewitt, K.: Glacier and landslide feedbacks to topographic relief in the Himalayan syntaxes, Proceedings of the National Academy of Sciences, 107, 5317, doi:10.1073/pnas.0907531107, 2010.

Lau, K. M., and Yang, S.: Climatology and Interannual Variability of the Southeast Asian Summer Monsoon, Advances in Atmospheric Sciences, 14, 141-162, 1997.

Li, X., Ding, Y., Liu, Q., Zhang, Y., Han, T., Jing, Z., Yu, Z., Li, Q., and Liu, S.: Intense Chemical Weathering at Glacial Meltwater-Dominated Hailuogou Basin in the Southeastern Tibetan Plateau, Water, 11, 10.3390/w11061209, 2019.

Li, Z., He, Y., Yang, X., Theakstone, W. H., Jia, W., Pu, T., Liu, Q., He, X., Song, B., Zhang, N., Wang, S., and Du, J.: Changes of the Hailuogou glacier, Mt. Gongga, China, against the background of climate change during the Holocene, Quaternary International, 218, 166-175, doi:10.1016/j.quaint.2008.09.005, 2010.

Liao, H., Liu, Q., Zhong, Y., and Lu, X.: Landsat-Based Estimation of the Glacier Surface Temperature of Hailuogou Glacier, Southeastern Tibetan Plateau, Between 1990 and 2018, remote sensing, 12, doi:10.3390/RS12132105, 2020.

Liu, G., Chen, Y., Zhang, Y., and Fu, H.: Mineral deformation and subglacial processes on ice-bedrock interface of Hailuogou Glacier, Chinese Science Bulletin, 54, 3318-3325, doi:10.1007/s11434-009-0289-x, 2009.

Liu, G., Zhang, B., Liu, Q., Zhang, R., Cai, J., Fu, Y., Yu, B., and Li, Z.: Monitoring Dynamics of Hailuogou Glacier and the Secondary Landslide Disasters Based on Combination of Satellite SAR and Ground-Based SAR, Geomatics and Information Science of Wuhan University, 44, 980-995, 2019a.

Liu, J., Zhang, J., Gao, B., Li, Y., Mengyu, L., Wujin, D., and Zhou, L.: An overview of glacial lake outburst flood in Tibet, China, Journal of Glaciology and Geocryology, 41, 1335-1347, 2019b.

Liu, Q., and Liu, S.: Seasonal evolution of the englacial and subglacial drainage systems of a temperate glacier revealed by hydrological analysis, Sci. Cold Arid. Reg, 2, 51-58, 2010.

Liu, Q., Liu, S., Zhang, Y., Wang, X., Zhang, Y., Guo, W., and Xu, J.: Recent shrinkage and hydrological response of Hailuogou glacier, a monsoon temperate glacier on the east slope of Mount Gongga, China, Journal of Glaciology, 56, 215-224, 2010.

Liu, Q., and Zhang, Y.: Studies on the dynamics of monsoonal temperate glaciers in Mt.Gongga: a review, Mountain Research, 35, 717-726, 2017.
Liu, Q., Liu, S., and Cao, W.: Seasonal Variation of Drainage System in the Lower Ablation Area of a Monsoonal Temperate Debris-Covered Glacier in Mt. Gongga, South-Eastern Tibet, Water, 10, 1050, 2018.
Liu, W., Carling, P. A., Hu, K., Wang, H., Zhou, Z., Zhou, L., Liu, D., Lai, Z., and Zhang, X.: Outburst floods in China: A review, earth science reviews, 197, doi:10.1016/J.EARSCIREV.2019.102895, 2019c.
Matsuoka, N.: Frost weathering and rockwall erosion in the southeastern Swiss Alps: Long-term (1994–2006) observations, geomorphology, 99, 353-368, doi:10.1016/J.GEOMORPH.2007.11.013, 2008.
McColl, S. T.: Paraglacial rock-slope stability, Geomorphology, 153-154, 1-16, doi:10.1016/j.geomorph.2012.02.015, 2012.
McColl, S. T., and Davies, T. R.: Large ice-contact slope movements: glacial buttressing, deformation and erosion, Earth Surface Processes and Landforms, 38, 1102-1115, 2013.
McColl, S. T.: Chapter 2 - Landslide Causes and Triggers, in: Landslide Hazards, Risks and Disasters, edited by: Shroder, J. F., and Davies, T., Academic Press, Boston, 17-42, 2015.
Miles, K. E., Hubbard, B., Miles, E. S., Quincey, D. J., Rowan, A. V., Kirkbride, M., and Hornsey, J.: Continuous borehole optical televiewing reveals variable englacial debris concentrations at Khumbu Glacier, Nepal, Communications Earth & Environment, 2, 12, doi:10.1038/s43247-020-00070-x, 2021.
Neckel, N., Loibl, D., and Rankl, M.: Recent slowdown and thinning of debris-covered glaciers in south-eastern Tibet, Earth and Planetary Science Letters, 464, 95-102, 10.1016/j.epsl.2017.02.008, 2017.
Oerlemans, J.: Climate sensitivity of Franz Josef Glacier, New Zealand, as revealed by numerical modeling, Arctic and Alpine Research, 29, 233-239, 1997.
Pan, B., Zhang, G., Wang, J., Cao, B., Geng, H., Zhang, C., and Ji, Y.: Glacier changes from 1966-2009 in the Gongga Mountains, on the south-eastern margin of the Qinghai-Tibetan Plateau and their climatic forcing, The Cryosphere, 6, 1087, 2012.
Reznichenko, N. V., Davies, T. R. H., Shulmeister, J., and Larsen, S. H.: A new technique for identifying rock avalanche–sourced sediment in moraines and some paleoclimatic implications, Geology, 40, 319-322, doi:10.1130/g32684.1, 2012.
Rodríguez-Rodríguez, L., González-Lemos, S., Ballesteros, D., Valenzuela, P., Domínguez-Cuesta, M. J., Llana-Fúnez, S., and Jiménez-Sánchez, M.: Timing of paraglacial rock-slope failures and denudation signatures in the Cantabrian Mountains (North Iberian Peninsula), Land Degradation & Development, 29, 3159-3173, doi:10.1002/ldr.3012, 2018.
Rowan, A. V., Quincey, D. J., Gibson, M. J., Glasser, N. F., Westoby, M. J., Irvine-Fynn, T. D. L., Porter, P. R., and Hambrey, M. J.: The sustainability of water resources in High Mountain Asia in the context of recent and future glacier change, Geological Society, London, Special Publications, 462, 189, doi:10.1144/SP462.12, 2018.
Salerno, F., Thakuri, S., D'Agata, C., Smiraglia, C., Manfredi, E. C., Viviano, G., and Tartari, G.: Glacial lake distribution in the Mount Everest region: Uncertainty of measurement and conditions of formation, global and planetary change, 92, 30-39, doi:10.1016/J.GLOPLACHA.2012.04.001, 2012.
Scherler, D., Wulf, H., and Gorelick, N.: Global Assessment of Supraglacial Debris-Cover Extents, Geophysical Research Letters, 45, 11,798-711,805, doi:10.1029/2018GL080158, 2018.
Schiefer, E., and Gilbert, R.: Reconstructing morphometric change in a proglacial landscape using historical aerial photography and automated DEM generation, Geomorphology, 88, 167-178, doi:10.1016/j.geomorph.2006.11.003, 2007.
Smith, W. D., Dunning, S. A., Brough, S., Ross, N., and Telling, J.: GERALDINE (Google earth Engine supRaglAciaL Debris INput dEtector) - A new Tool for Identifying and Monitoring Supraglacial Landslide Inputs, Earth Surf. Dynam. Discuss., 2020, 1-21, doi:10.5194/esurf-2020-40, 2020.
Su, Z., and Shi, Y.: Response of monsoonal temperate glaciers to global warming since the Little Ice Age, Quaternary International, 97-98, 123-131, 2002.
van Woerkom, T., Steiner, J. F., Kraaijenbrink, P. D. A., Miles, E. S., and Immerzeel, W. W.: Sediment supply from lateral moraines to a debris-covered glacier in the Himalaya, Earth Surf. Dynam., 7, 411-427, doi:10.5194/esurf-7-411-2019, 2019.
Wang, P., Li, Z., Li, H., Wang, W., Wu, L., Zhang, H., Huai, B., and Wang, L.: Recent Evolution in Extent, Thickness, and Velocity of Haxilegen Glacier No. 51, Kuytun River Basin, Eastern Tianshan Mountains, arctic antarctic and alpine research, 48, 241-252, doi:10.1657/AAAR0014-079, 2016.
Williams, H. B., and Koppes, M. N.: A comparison of glacial and paraglacial denudation responses to rapid glacial retreat,

Annals of Glaciology, 60, 151-164, doi:10.1017/aog.2020.1, 2020.
Xu, Q., Shang, Y., AschTheo, v., Wang, S., Zhang, Z., and Dong, X.: Observations from the large, rapid Yigong rock slide – debris avalanche, southeast Tibet, canadian geotechnical journal, 49, 589-606, doi:10.1139/T2012-021, 2012.
Xu, X., Ma, D., He, D., and Huang, H.: Analysis on hydro-thermal combination of debris flow occurrence in Mt. Gongga region, Mountain Research, 431-437, 2007.
Yao, T., Thompson, L., Yang, W., Yu, W., Gao, Y., Guo, X., Yang, X., Duan, K., Zhao, H., Xu, B., Pu, J., Lu, A., Xiang, Y., Kattel, D. B., and Joswiak, D.: Different glacier status with atmospheric circulations in Tibetan Plateau and surroundings, Nature Climate Change, 2, 663-667, 10.1038/NCLIMATE1580, 2012.
Yao, T., Xue, Y., Chen, D., Chen, F., Thompson, L., Cui, P., Koike, T., Lau, W. K. M., Lettenmaier, D., Mosbrugger, V., Zhang, R., Xu, B., Dozier, J., Gillespie, T., Gu, Y., Kang, S., Piao, S., Sugimoto, S., Ueno, K., Wang, L., Wang, W., Zhang, F., Sheng, Y., Guo, W., Ailikun, Yang, X., Ma, Y., Shen, S. S. P., Su, Z., Chen, F., Liang, S., Liu, Y., Singh, V. P., Yang, K., Yang, D., Zhao, X., Qian, Y., Zhang, Y., and Li, Q.: Recent Third Pole's Rapid Warming Accompanies Cryospheric Melt and Water Cycle Intensification and Interactions between Monsoon and Environment: Multidisciplinary Approach with Observations, Modeling, and Analysis, Bulletin of the American Meteorological Society, 100, 423-444, doi:10.1175/BAMS-D-17-0057.1, 2019a.
Yao, T., Yu, W., Wu, G., Xu, B., Yang, W., Zhao, H., Wang, W., Li, S., Wang, N., Li, Z., Liu, S., and You, C.: Glacier anomalies and relevant disaster risks on the Tibetan Plateau and surroundings, chinese science bulletin, 64, 2770-2782, doi:10.1360/TB-2019-0246, 2019b.
Yao, X., Liu, S., Sun, M., and Zhang, X.: Study on the glacial lake outburst flood events in Tibet since the 20th Century, Journal of Natural Resources, 29, 1377-1390, 2014.
Zhang, W.: Some features of the surge glacier in the Mt. Namjagbarwa, Mountain Research, 3, 234-238, 1985.
Zhang, Y., Fujita, K., Liu, S., Liu, Q., and Wang, X.: Multi-decadal ice-velocity and elevation changes of a monsoonal maritime glacier: Hailuogou glacier, China, journal of glaciology, 56, 65-74, doi:10.3189/002214310791190884, 2010.
Zhu, Z.: On Characteristics of Visitor Flow to Hailuogou Glacier Forest Park in Sichuan, Journal of Huizhou University, 35, 66-69+80, 2015.
Zou, Q., Cui, P., Jiang, H., Wang, J., Li, C., and Zhou, B.: Analysis of regional river blocking by debris flows in response to climate change, Science of The Total Environment, 741, 140262, doi:10.1016/j.scitotenv.2020.140262, 2020.

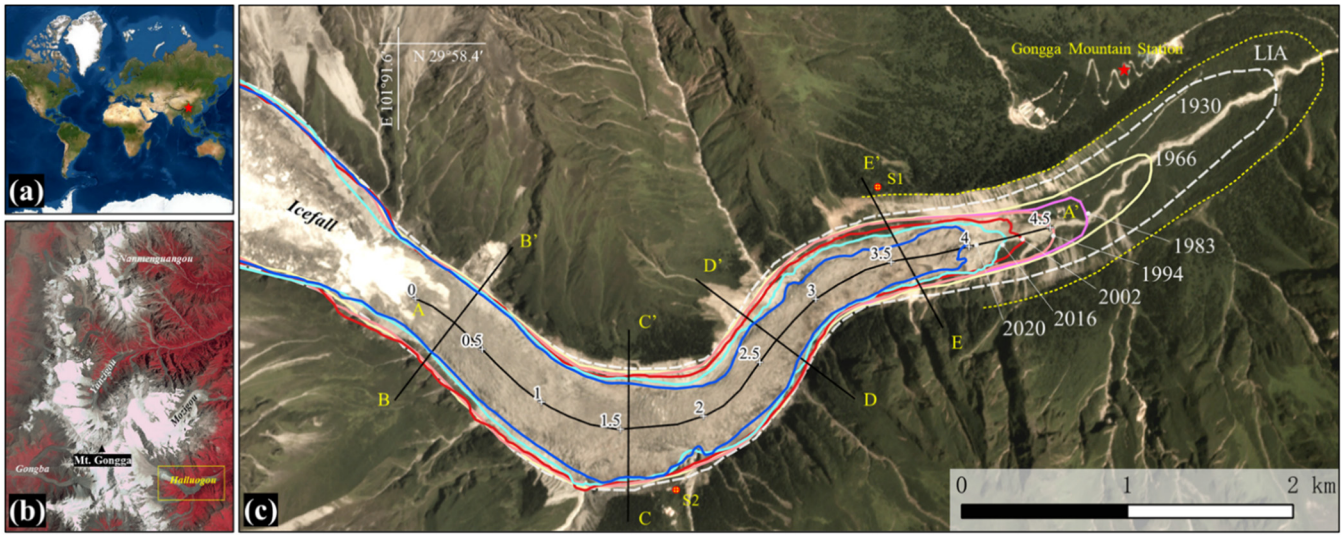

Figure 1: Map showing the location of Mt. Gongga (red star), the background image is from ESRI's world basemap (a), several large glaciers around the peak of Mt. Gongga based on Landsat image (b), and retreating history of HLG since the Little Ice Age based on PlanetScope imagery (c). S1 and S2 are tourist sightseen stands on both sides of lateral moraines, and the red star indicates the location of Gongga Mountain Station. Longitudinal (A-A') and transverse (B-B', etc.) lines are set to examine the variation of flow velocities and surface elevations (Fig. 3) of the ice tongue.

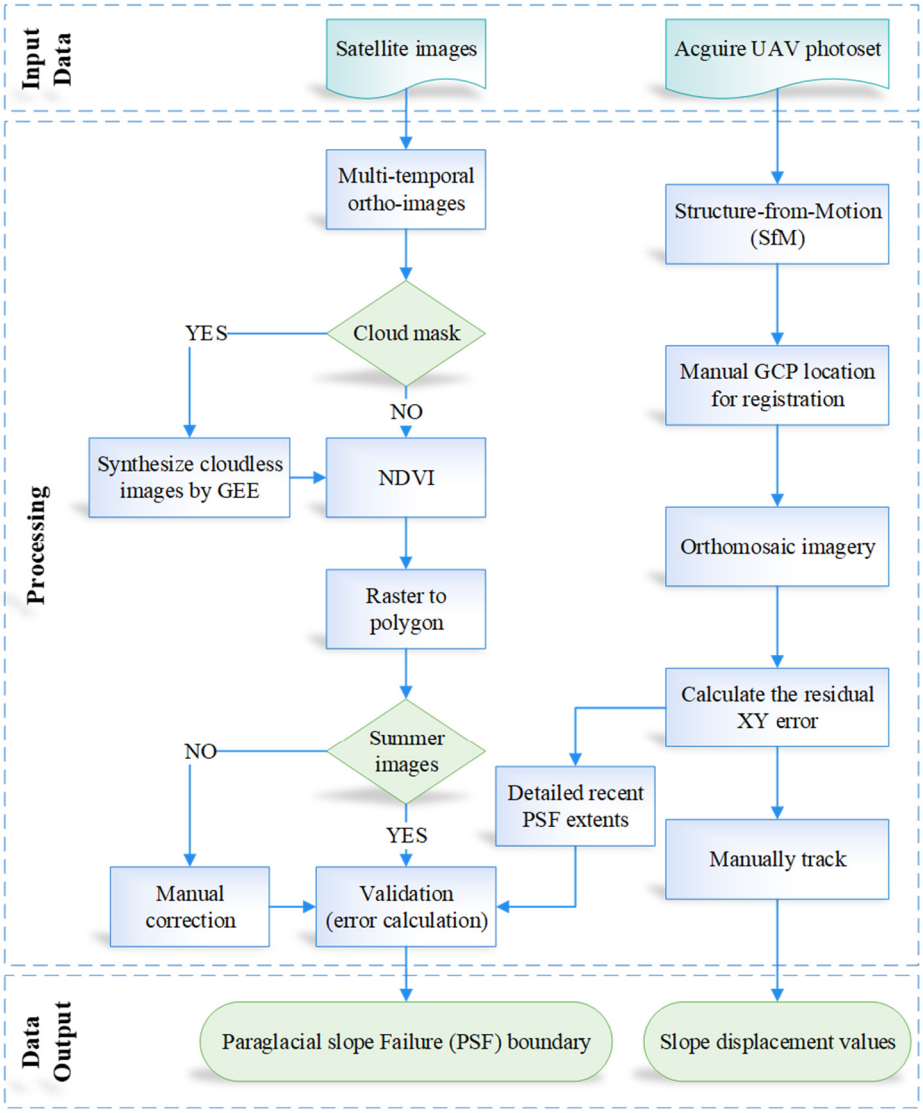

Figure 2: Workflow of the methodology followed to mapping the PSFs (changes) and tracking the displacement from multi-temporal image data.

840

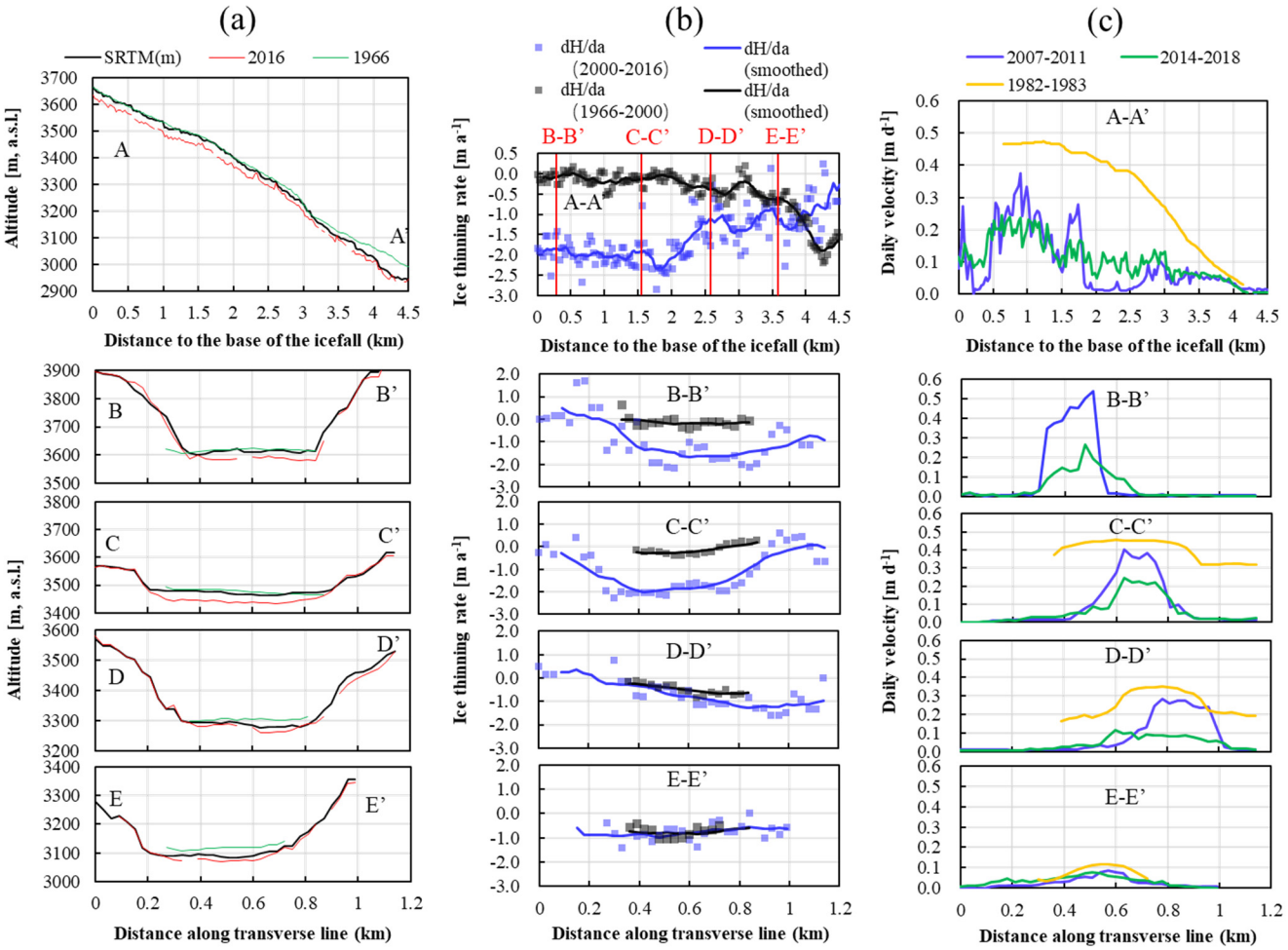

Figure 3: Comparison of ice surface elevations, average annual ice thinning rates (Brun et al., 2017), and velocity changes (Liu et al., 2019a;Zhang et al., 2010) along with profiles A-A' to E-E' in Figure 1.

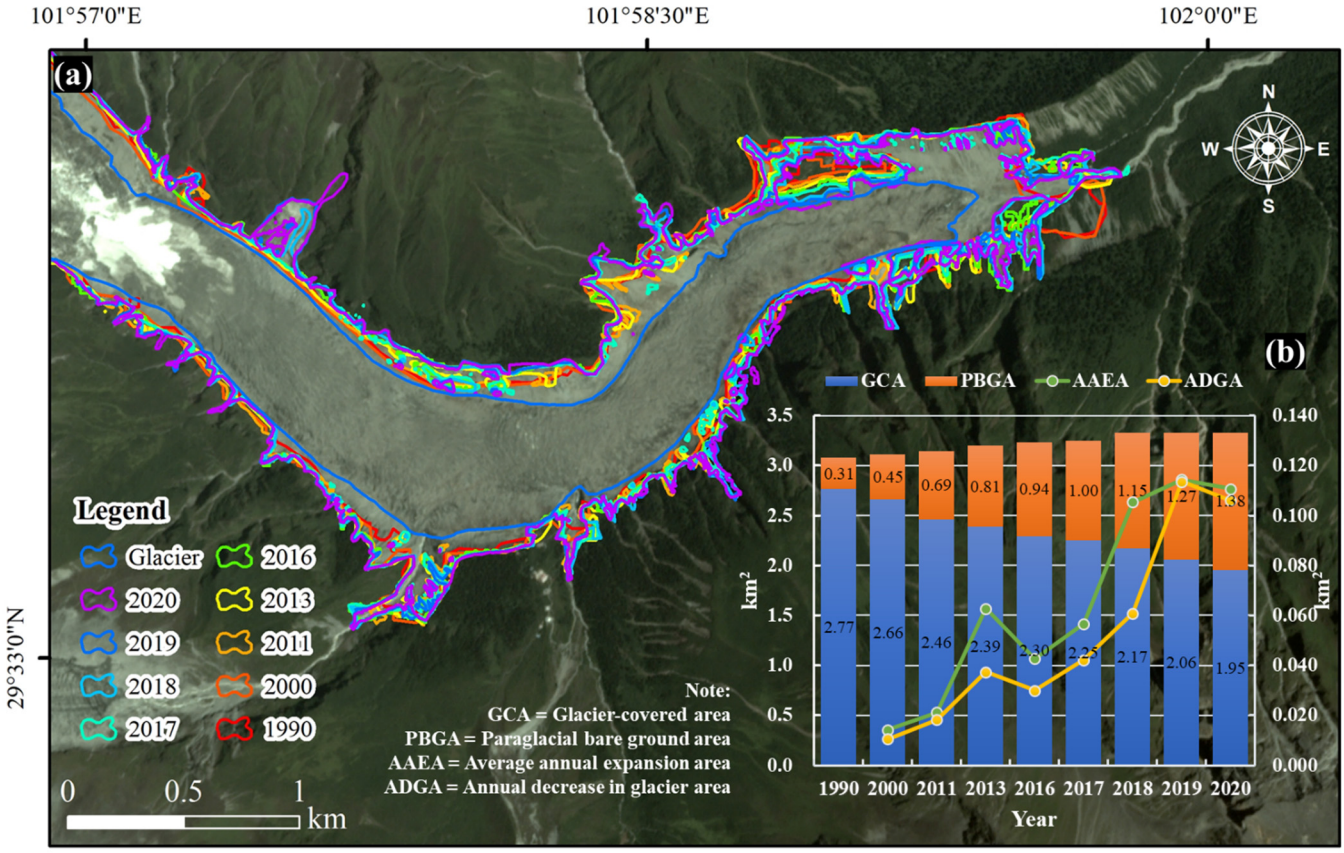

Figure 4: (a) Mapping results of PSFs in the HLG between 1990 and 2020. The glacier boundary (blue line) is mapped by a PlanetScope image acquired on August 16, 2019 (background). (b) Changes of the glacier-covered area (GCA, blue) and the paraglacial bare ground area (PBGA, orange) between 1990 and 2020. The green line indicates the average annual expansion area (AAEA) of PBGA. The yellow line indicates the annual decrease in glacier area (ADGA).

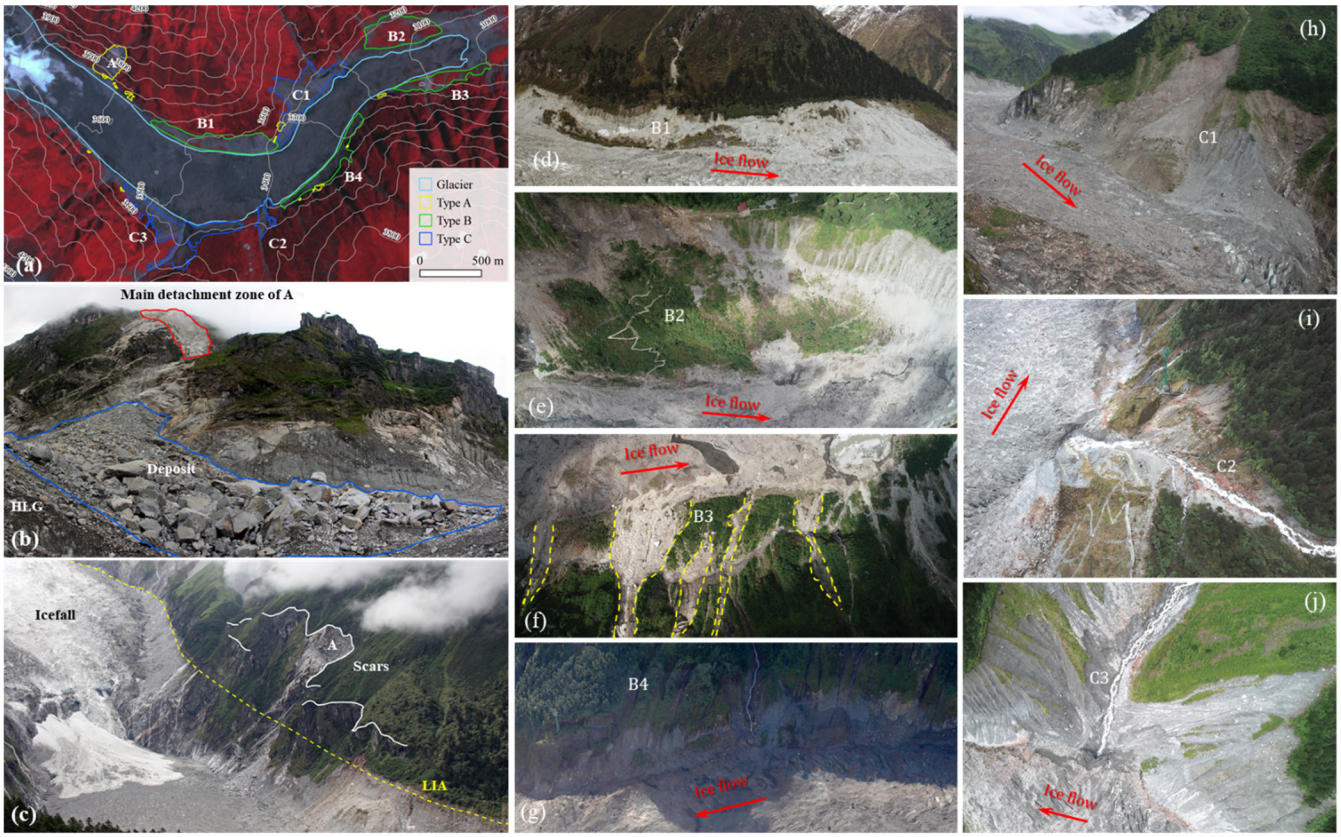

Figure 5: (a) The distribution of three types of PSFs based on Landsat image. (b) The particulars of type A failures in the upper part of the HLG's ice tongue. Main detachment zone (red), Deposit (blue). (c) The scars (white lines) surrounding the rockfall A. Subplots (d, e, f, and g) and (h, i and j) are closer photographs of Type B and Type C failures, respectively, field photo by Qiao Liu.

855 **(this figure was removed to Supplementary file)**

(this figure was removed to Supplementary file)

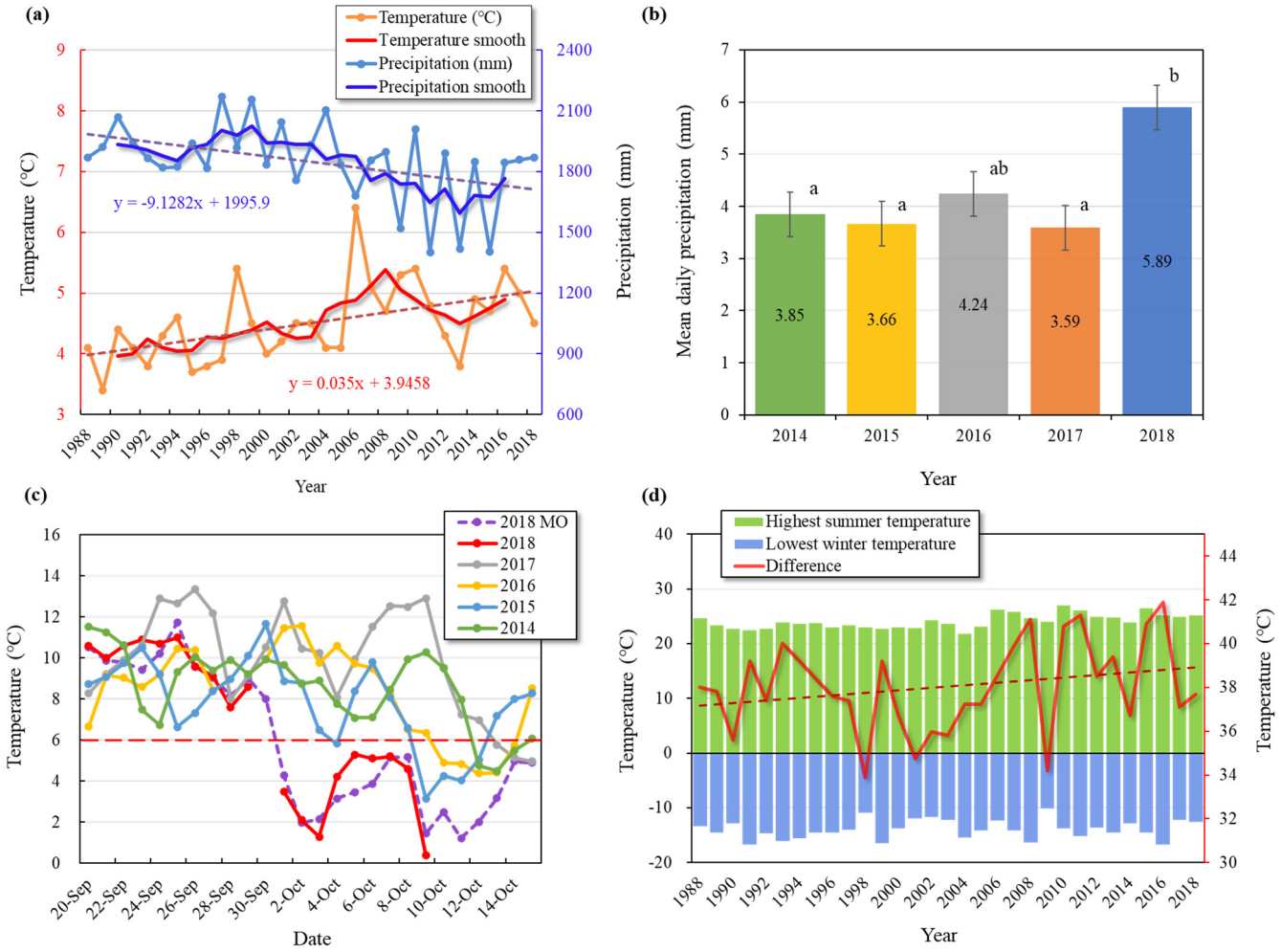

Figure 6: Meteorological data. (a) Mean annual air temperature (orange) and annual precipitation (blue) were recorded at the 3000 m station. The temperature data for 2017 are from manual observations. Between 1990 and 2016, the moving average for temperature and precipitation has been calculated. (b) Differences in the mean daily precipitation between 5-20 Oct 2018 and 5-20 Oct 2014-2017. Analysis of Variance (ANOVA) was used to investigate the difference of mean daily precipitation between five years, it found that mean daily precipitation in 2018 was significantly higher than that in 2014, 2015, and 2017 ($p<0.05$). (c) Differences in the daily mean temperature between September to October 2018 and September to October 2014-2017, MO means manual observation. (d) The average of the highest summer temperature (green bar) and lowest winter temperature (blue bar) of each year, and their differences (red line).

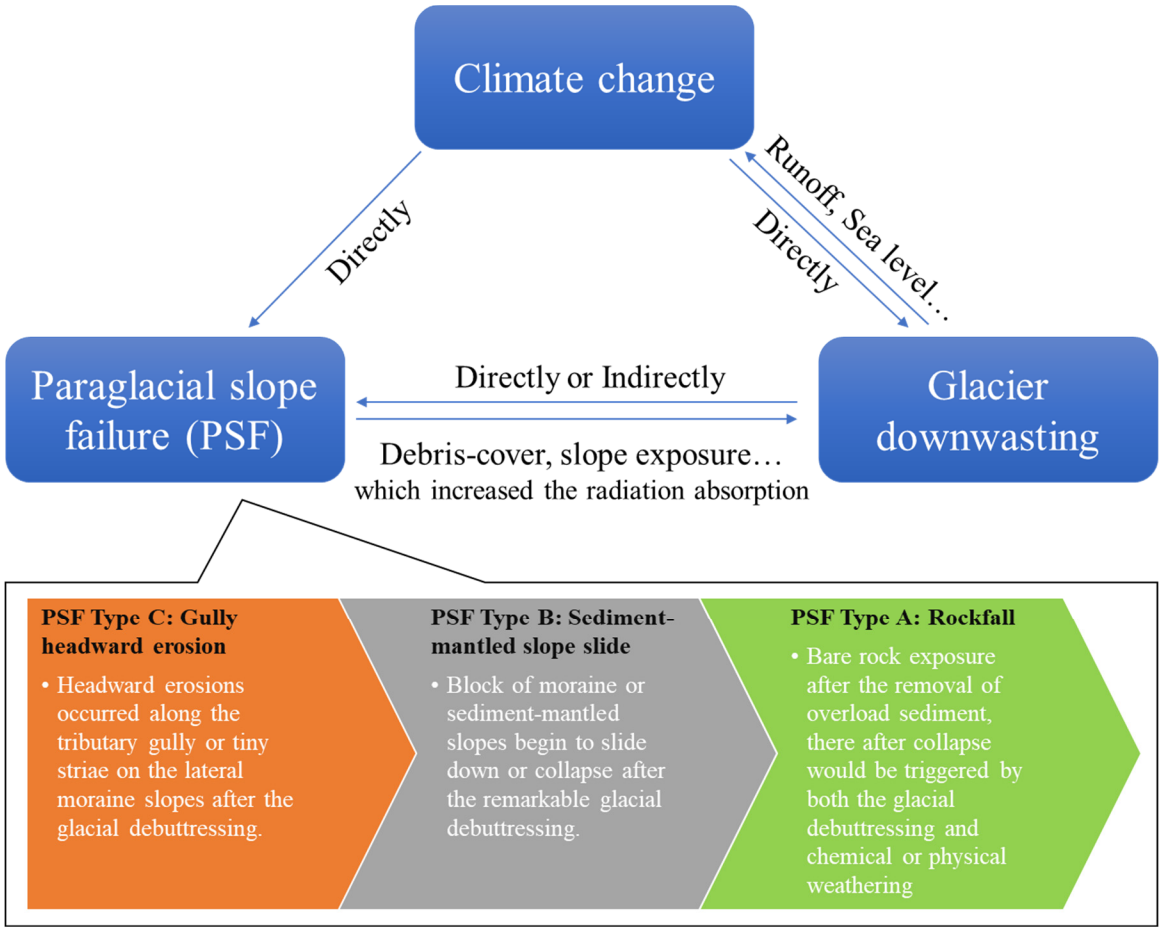

Figure 7: The relationship among PSF, ongoing climate change, and glacier downwasting. Climate change can directly trigger the PSF through extreme precipitation and sudden increase/decrease of temperature or indirectly trigger the PSF by glacier downwasting, which can also be used as a preparatory factor to indirectly trigger PSF (e.g., rockfalls). At the same time, many debris fell into the glacier surface, increasing the range and thickness of the supraglacial debris-cover, which in turn affected the surface energy balance for melting and therefore downwasting rate of the glacier, which will thus influence the rate of runoff generation and its contribution to the sea level rise from glacierised catchments.

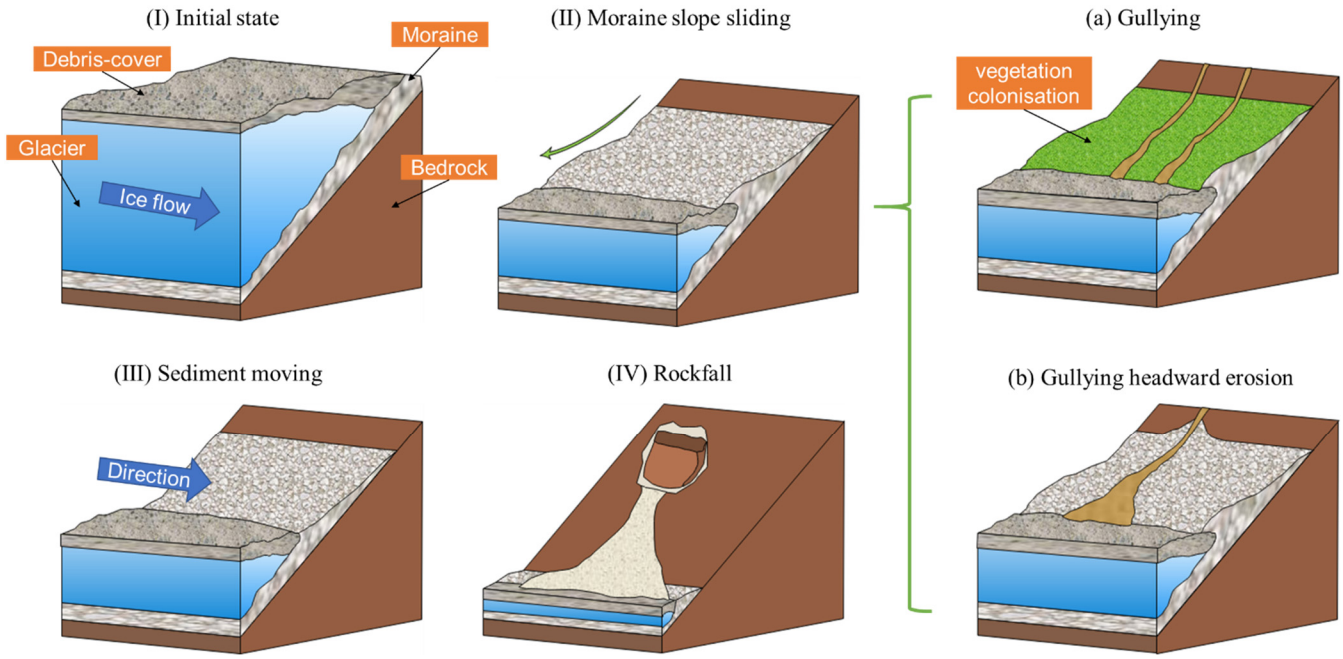

875 **Figure 8: A conjectural model of paraglacial slope evolution and sediment delivery.**

Table 1: Satellite/UAV data used to map the PSFs extents

Sensor Type	Acquiring Date (YYYY.MM.DD)	Near Infrared (NIR)	Red (R)	Spatial Resolution (m)
Landsat TM	1990.07.08/2000.08.20	Band4	Band3	30
Sentinel 2	2016.05.05/2018.08.23	Band8	Band4	10
RapidEye	2011.08.29/2013.05.26/2014.04.16/2015.04.03	Band5	Band3	5
PlanetScope	2017.07.17/2019.08.16/2020.08.20	Band4	Band3	3.125
Google Earth	2002.10.12 (SPOT5)	Band3	Band2	2.5
DJ-UAV	2016.08.31/2017.06.07/2018.08.19/2019.05.15	-	-	0.1

Table 2: Dimensions of PSFs in the study area. We selected periods of high-resolution images with the most obvious terrain changes, the PlanetScope image (2019) for Type A, the UAV images (2016-2019, Fig. S1) for Type B, the PlanetScope, RapidEye, and © Google Earth images (2002, 2011, 2014, 2015, 2019) for Type C (locations are shown in Fig. 5a).

PSFs type ID	Length (m)	Width (m)	Area (m^2)	Displacement speed / Upper edge retreat rate ($cm\ d^{-1}$)	Increase in exposed area (m^2)
A	200	283	47,000	-	-
B1	1035	114	112,424	1.96±0.04/-	12,125 (2016-2019)
B2	644	262	122,738	2.63±0.04/-	7,414 (2016-2019)
B3	805	132	63,241	1.65±0.04/-	8,528 (2016-2019)
B4	993	103	73,270	1.66±0.04/-	10,130 (2016-2019)
C1	849	312	139,135	-/3.39±0.20	45,499 (2011-2019)
C2	164	269	24,248	-/0.76±0.11	11,923 (2002-2019)
C3	1097	512	160,474	-/1.15±0.15	50,989 (2002-2019)